Title

Solenoid Design Enabling the Direct Electron Imaging of Microchannel Plate Amplifiers

Author

Ricci, Jordan Tyler

Publication Date

2024

Peer reviewed|Thesis/dissertation

Solenoid Design Enabling the Direct Electron Imaging of Microchannel Plate Amplifiers

By

JORDAN T. RICCI
THESIS

Submitted in partial satisfaction of the requirements for the degree of

MASTER OF SCIENCE

in

Electrical and Computer Engineering

in the

OFFICE OF GRADUATE STUDIES

of the

UNIVERSITY OF CALIFORNIA

DAVIS

Approved:

_____

Charles E. Hunt

_____

Juan Sebastian Gomez-Diaz

_____

Klaus van Benthem

Committee in Charge

2024

Dedicated to my family, as a small way of repaying them for their support and investment in me. This achievement is not mine alone; all of you have shown and taught me firsthand the true meaning of hard work. This was made possible because of the endless love you have always given me. I would not be here today without you all.

I specifically dedicate this thesis to my brothers, Alex and Dominic. Boys, when you set your mind to something, there is nothing that you cannot achieve.

Acknowledgements

First and foremost, I would like to thank Professor Charles E. Hunt for this incredible opportunity, his guidance and support, and for the wealth of knowledge that he has imparted to me over the years. I would like to sincerely thank Terry Hilsabeck, who was a tremendous mentor to me: I certainly would not have gained the technical knowledge for this thesis without him. I would also like to express my sincere thanks to Arthur Carpenter for the opportunity and for his always reliable support.

I would also like to thank Bernie Vancil for his immense generosity and willingness to help with our experimental issues. I would like to thank Robby Beard for his huge help in the development of the pulsing circuitry. This research was made possible by the funding from Lawrence Livermore National Laboratory and the supervision of Arthur Carpenter. In addition, the magnetic field data collected was made possible due to the generosity of General Atomics.

Finally, I would like to recognize Ryan Gloekler and M.A. Mort for being the best lab mates that I could have ever asked for. You are both brilliant minds; it was an absolute pleasure to work, learn, and grow alongside you.

Abstract

A solenoid was built and installed in an ultra-high vacuum environment which guides and condenses electrons from the output charge cloud of a microchannel plate amplifier into a high-intensity, condensed electron beam. A low-intensity electron signal was input into the signal amplifier, where the external magnetic field generated by the solenoid resulted in a higher flux of electrons reaching the electron detector. High-current hardware was developed which pulses the solenoid for 10-ms at a peak current of 14.2 A, generating a peak magnetic field of 285.2 Gauss. The applied magnetic field increases the dynamic range of the electron image, with the observed intensity range increasing by a factor of up to 3.95. The average image intensity increased by a factor of up to 15.0 while the solenoid was pulsed. For a fixed microchannel plate bias, the accelerating grid and phosphor imaging plate high-voltage biases were swept to characterize the beam under different experimental conditions. The raw intensity distributions of the beams were profiled and fit to Gaussian distributions. Beams under the different experimental biases were imaged, and ellipses were fit to their intensity distributions. One standard deviation above each sample's mean intensity, the resultant beams had an average beam size of 82.3 mm^2, ellipse ratio of 0.77, offset from the origin on 4.38 mm, and rotation of 130.5°. The different beam images were post-processed, analyzed, and overlayed relative to each other using computer-aided design software to illustrate the relative beam sizes and intensities on the phosphor screen.

Chapter 1

1.1: Background

In imaging systems with weak input signals, signal amplifiers are utilized to enhance an imager's performance. In the context of electron-imaging, microchannel-plate amplifiers (MCPs) are commonly used due to their high gain of 10^4 - 10^7 and sub-100-picosecond temporal resolution [1]. When using MCPs in a well-designed electron imaging system, the primary goal is to use an electron detector to collect an amplified electron signal that accurately reflects the signal incident to the MCP. However, as a byproduct of avalanche electron multiplication in MCPs, high-energy electrons exit the device at angles as high as 20-degrees, resulting in an electron output charge cloud [2]. As a plume of high-energy electrons exit the device at large angles, it is possible that there will be a loss of signal at the electron detector, reducing the amount of signal amplification and potentially leading to the loss of information in the final electron image.

Since MCP pores are small, with typical diameters of 25-100 μm [1], it is likely that multiple pores will simultaneously receive a signal, amplify it, and consequently produce their own output charge cloud. The separate charge clouds across different MCP pores can overlap and further interact with each other. Therefore, while MCPs are advantageous due to their high gain, they pose a serious problem due to the significant image distortion that the overlapping charge clouds can cause between the original input signal and the final electron image. The question persists: what can be done to mitigate the adverse byproducts of an MCP signal amplifier?

External electromagnetic fields can be applied to guide MCP output electrons to the detector, increasing the amount of signal received at the imaging plane. The forces generated by the electromagnetic fields act on and condense the size of each MCP pore's output charge cloud.

The goal of applying these external fields is to reduce the amount of overlap between neighboring output charge clouds. This will ultimately reduce the amount of image distortion at the detector and will improve the overall quality of the resulting electron image.

1.2: Research Description

Presented here is the design, modeling, and experimental testing of a solenoid designed to guide MCP output electrons to an electron detector. The solenoid was implemented under UHV along with a phosphor imaging plate as a proof-of-concept. In future work, a high-speed, direct electron imager would be used in place of the phosphor screen to quantify temporal response. An electron beam was used as the input signal to the MCP. The solenoid was pulsed for 10 ms with a peak current of 14.2 A. A high-voltage potential difference was established between the MCP and phosphor imaging plate, where the electric field accelerates electrons towards the detector.

1.3: Microchannel Plate Amplifiers (MCPs)

A microchannel plate is a glass structure consisting of an array of microchannels, as shown in Figure 1. The functioning principle is that incident particles or radiation collide with the inner channel walls, creating secondary particle emission. The channels are slightly angled, typically around 8-degrees [1], so that incident particles or radiation have a higher probability of colliding with the channel walls. The device and its channel walls are made of a lead glass material due to the material's high secondary electron emission [3]. The front and back faces of the device are coated in Nichrome, a Nickel-Chromium alloy. This metallic coating forms electrodes to create an electric field across the device and throughout the channels.

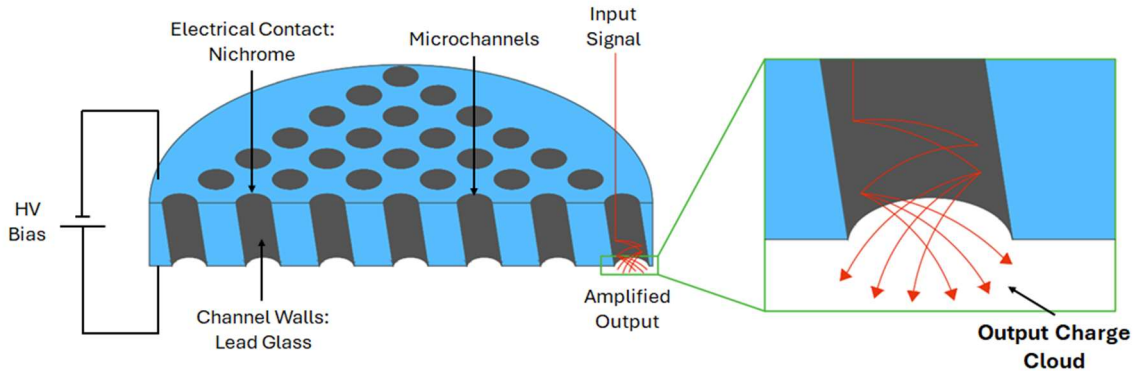

Figure 1: Structure of an MCP (Figure adapted from [4]).

When a high-voltage bias is applied across the MCP, secondary electrons are swept towards the back end of the device. Before the electrons can exit the back end of the MCP, they repeatedly recollide with the channel walls. This results in a cascading electron multiplication effect inside the microchannels, as shown in Figure 1. Electrons can exit an MCP pore at an array of different energies and angles, depending on their path taken through the channels. Figure 2 displays a measured profile of the initial energy and angle distributions of electrons exiting an MCP.

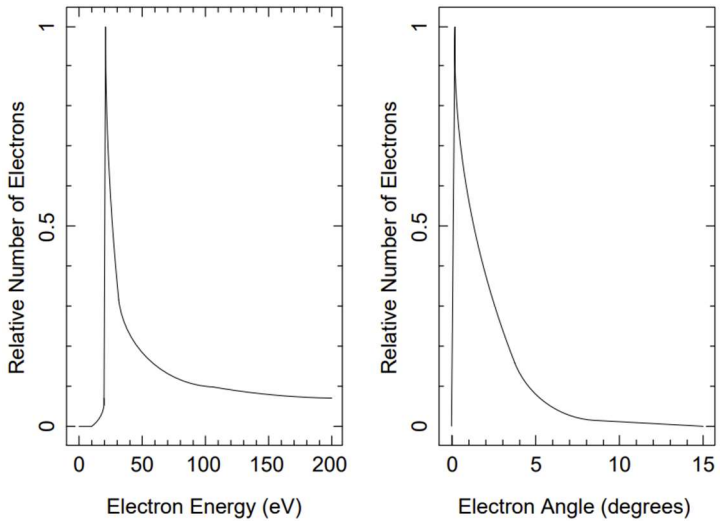

Figure 2: Typical MCP initial electron energy and angle distribution (Figure adapted from [2]).

1.4: Electron Optics

1.4.1: Electron Optics

Similar to how traditional light optics studies the behavior of light, electron optics analyzes the behavior of electrons, specifically the influence that the electromagnetic forces have on electron trajectories. In the presence of electromagnetic fields, electrons are acted on by the forces generated by the fields, given by [5]:

$$\vec{F} = \vec{F}_E + \vec{F}_m = -e[\left(\frac{d\vec{V}}{dx} + \frac{d\vec{V}}{dy} + \frac{d\vec{V}}{dz}\right) + (\vec{v}\ x\ \vec{B})]$$

A set of differential equations governing electron motion is deduced as follows [5]:

$$m_e \frac{d^2x}{dt^2} = -e[\vec{E}_x + \left(B_y \frac{dz}{dt} - B_z \frac{dy}{dt}\right)]$$

$$m_e \frac{d^2y}{dt^2} = -e[\vec{E}_y + \left(B_z \frac{dx}{dt} - B_x \frac{dz}{dt}\right)]$$

$$m_e \frac{d^2z}{dt^2} = -e[\vec{E}_z + \left(B_x \frac{dy}{dt} - B_y \frac{dx}{dt}\right)]$$

The solutions to the differential equations reveal the position of an electron traveling through the fields at a given time. The general shape of the electron's path is a helix; however, the stretching or compression of the helix heavily relies on the magnitudes and directions of both fields. In particular, the directions of the fields relative to one another dictate the shape and properties of the helix. The magnetic field gives the electron trajectory its helical shape, whereas the electric field is an accelerating field that can stretch or compress the helix, depending on the direction of the field [5].

The initial velocity of an electron directly influences the pitch and radius of its helical path. If an electron drifts in the Z-direction, the Z-component of its initial velocity (V_{0z})

contributes to the pitch (h) of the helix, whereas the perpendicular component ($V_{0\perp}$) contributes to the radius (R) of the helix [5]:

$$h \propto V_{0z}\,;\; R \propto V_{0\perp} = \sqrt{V_{ox}^2 + V_{0y}^2}$$

Assuming that there is no magnification or demagnification of the original signal, for a proper electron image to be formed, an electron originating from the point (X_0, Y_0) in the XY object plane must preserve the same (X_0, Y_0) position in the XY imaging plane [5]. For this to occur, an electron detector should be placed at a distance which is an integer multiple of the electron's pitch. However, when multiple electrons originate from a point source and have a range of different V_{0z}, such as the output energy distribution of an MCP, there will inevitably be image distortion at the imaging plane because most electrons will have different pitches. Not all of their pitches will coincide with the chosen imager spacing. When there is image distortion, an electron will be at a new position (X_1, Y_1) in the XY imaging plane opposed to its original position (X_0, Y_0), which would have formed a proper electron image. Such an electron is a distance (d) away from its origin point in the XY plane:

$$d = \sqrt{(X_1 - X_0)^2 + (Y_1 - Y_0)^2}$$

To mitigate the negative consequence of the MCP output electron energy distribution, rather than trying to deliberately choose the object-to-imager distance, the radius of an electron's helical trajectory can be minimized. To minimize the radius of an electron's helical trajectory, the Z-component of the magnetic field (B_z) can be increased. This suggests that limiting the size of an MCP pore's output charge cloud can be accomplished by generating a magnetic field in the Z-direction. In this research, a solenoid is used to accomplish this task.

1.4.2: Solenoids

A solenoid is a collection of current loops which generates a highly directional and uniform magnetic field. The magnetic field that a solenoid produces can be explained by Ampère's law [6], stating that the line integral of the magnetic flux density (B) over a closed path (C) is equal to the product of the total current passing through that closed path and the permittivity of free space:

$$\oint_c B \bullet dl = \mu_0 I$$

Consequently, via Ampère's law, a single closed current loop with wire width (l) and radius (R) has a resultant magnetic flux density in the $\hat{z}$-direction:

$$B = \hat{z}\frac{\mu_0 I}{l}$$

Multiple turns can be wound to create a solenoid with radius (R). While the solenoid is helical in shape, it can be thought of as a collection of individual current loops cascaded in series [6]. Extending the results from a single current loop, the total magnetic flux density can be integrated over the total length of the coil (L), dictated by the total number of turns (N). Assuming the coil is a "long solenoid," meaning the length-to-radius ratio is much greater than one, integration results in a field magnitude [6] of:

$$B = \hat{z}\frac{\mu_0 NI}{L}, (\frac{l}{r} \gg 1)$$

The magnetic field flux density is thus proportional to the number of turns in the coil, suggesting that the field contribution from each individual current loop is additive in the resultant field magnitude. The solenoid field equation is an approximation which can be applied everywhere

inside the bounds of the coil excluding the endpoints of the coil [6], as the distribution of the field magnitude is Gaussian with a peak field at the center of the coil lengthwise. Figure 3 shows the overall field distribution for a solenoid, with highly directional field lines inside the bounds of the coil. At the end of coil where current exits the device, the field lines curl away from the solenoid and back towards the end of the device where current enters.

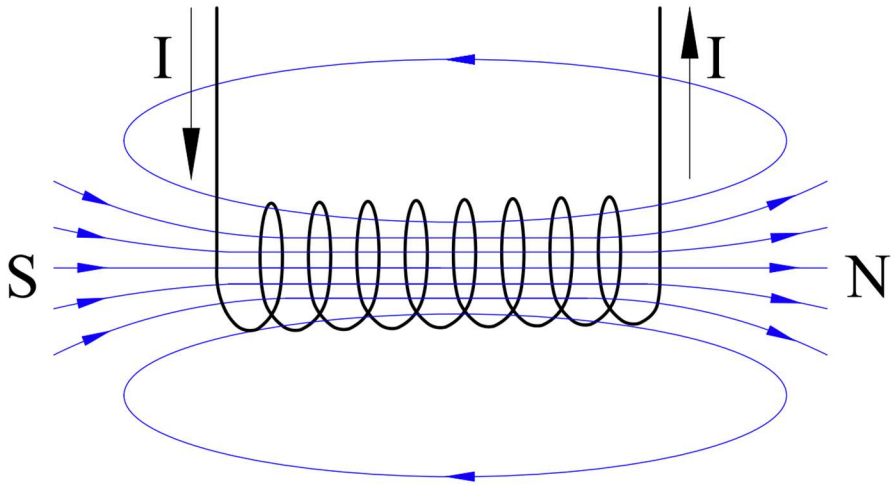

Figure 3: Typical magnetic flux density (B) distribution of a solenoid (Figure adapted from [6]).

In its most simple form, a solenoid is nothing more than an inductor. The solenoid stores energy in the form of a magnetic field in the surrounding area of the device, resisting any instantaneous change in current. The total inductance of a solenoid is given by the following expression [6]:

$$L = \frac{\mu_0 N^2}{L}$$

Chapter 2

2.1: Solenoid Design Parameters

A solenoid was designed with the goal of generating a minimum peak field of 200 Gauss. The constructed device is shown in Figure 4. The device consists of a coil made of 18 AWG polyimide-coated solid copper wire, bound to an enclosure made of polyether ether ketone (PEEK). The thick wire gauge was chosen because of its high current rating of 10 A. In addition, an overly thick wire gauge ensures that the coil can withstand high temperatures, as a device under UHV will have much lower heat dissipation due to the lack of surrounding gasses in the vacuum chamber. PEEK was the material chosen for the enclosure due to its UHV-compatibility and machinability.

Figure 4: Assembled solenoid mounted on PEEK enclosure.

The device was designed so that its center coincides with the optical axis of the electron beam, in-line with the center of the vacuum flange. Along with housing the solenoid, the enclosure was designed to create a confined region for electron drift from the MCP to the imager, effectively setting the MCP-to-imager spacing. The coil length was chosen to be 8.25

cm. This specific length was selected because shorter solenoid lengths produce larger field strengths. At the same time, the chosen distance is sufficient to prevent high-voltage arcing between the backside of the MCP and the detector, which are both biased at high-voltages. The highest current that was believed to be feasible in the system was 12.5 A; therefore, the number of turns needed to produce a field of at least 200 Gauss was calculated to be 105. An additional 39 turns were implemented due to the available space on the enclosure. The properties of the fabricated device are summarized in Table 1. More information about the structure and dimensions of the fabricated device can be found in Appendix A.

Number of Turns	144
Target Current	12.5 A
Coil Length	8.25 cm
Calculated Peak Field	274 Gauss
Calculated Coil Inductance	0.36 mH

Table 1: Design parameters and calculations of the constructed device.

2.2: Solenoid Magnetic Field Modeling

2.2.1: FEMM Model Overview

A model of the solenoid was developed using Finite Element Method Magnetics (FEMM) software [7] with the goal of obtaining an accurate 3-dimensional profile of the magnetic field inside of the vacuum chamber. Having a detailed model of the magnetic field distribution enables the further analysis of electron trajectories within the drift region. This software was chosen as it is designed for magnetics problems and has a built-in coil feature. In addition, the program's numerical methods formulated by the Finite Element Method produce sufficiently accurate solutions compared to values observed in practice [7].

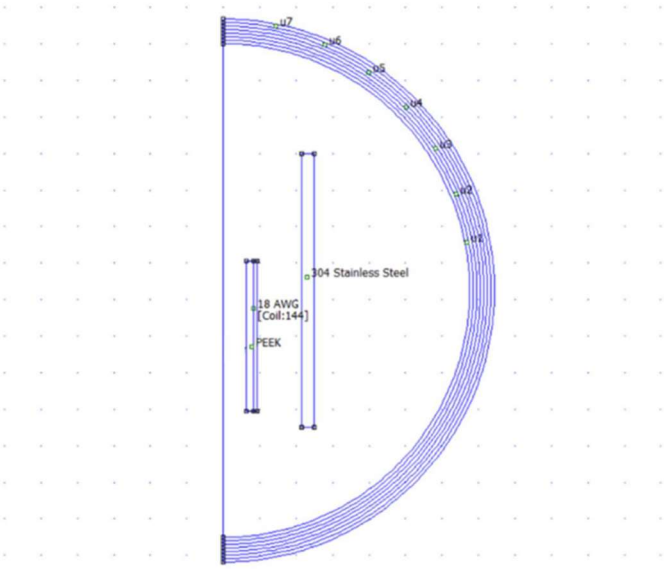

Figure 5: FEMM simulation layout (grid size = 2 cm).

2.2.2: FEMM Simulation Setup

The coil, PEEK enclosure, and 304-Strainless Steel vacuum chamber are all cylindrical and centered about the optic axis. Due to this symmetry, the simulation can be reduced to an axisymmetric 2-dimension simulation, whose results are valid in 3 dimensions when rotated about the optic axis. In the 2-dimensional model each component is rectangular, since the intersection of a 2-dimensional plane from the optic axis to each cylindrical component is a rectangle. The model setup is shown in Figure 5 and the specific parameters of the simulation are listed in Appendix B.

2.2.3: FEMM Modeling Results

The software produced a 2-dimensional representation of the system's magnetic flux density, shown in Figure 6. The magnetic field profile from the simulation exhibits the expected behavior of a solenoid, with a strong and uniform field inside the bounds of the coil. Parallel field lines inside the solenoid highlight that the field's direction is highly uniform, as directed

towards the detector. The magnetic field lines curl away from the end of the coil where current exits the device, curling back towards the end where current reenters. The curled field lines at the edges of the coil are caused by an abrupt lack of current loops, impairing the magnetic field's uniformity. There is a gradient in the field magnitude between the outer limit of the coil and the vacuum chamber; however, Figure 6 suggests that the field magnitude is relatively weak, with a near-zero field magnitude at the inner vacuum chamber boundary. The simulation was run at 14.2 A: the measured peak current of the device.

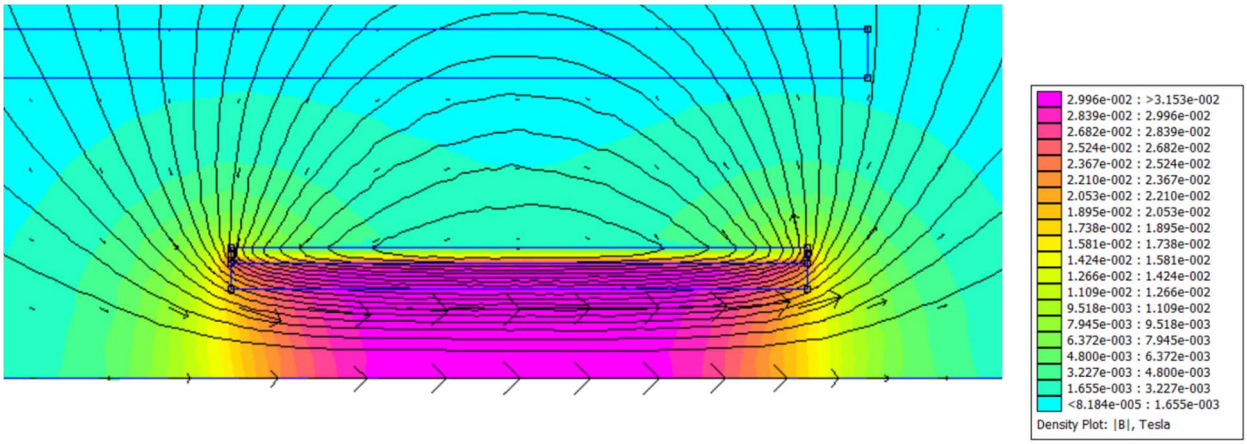

Figure 6: Magnetic field flux density plot |B|, I_{peak}=14.2 A.

The peak magnetic field along the optic axis was modeled and is shown in Figure 7. The field was monitored between the bounds of the coil, extending an additional 0.875 cm past both ends of the coil. The magnetic field profile exhibits a gaussian distribution, with a peak field of 286 Gauss at the center of the coil lengthwise. The distribution has a full width at half maximum of 8.42 cm, notably surpassing the 8.25 cm length of the solenoid. The target field of 200 Gauss is reached within the inner 7.45 cm of the solenoid, with a field magnitude of 143 Gauss at the limits of the coil. In addition, a field magnitude of 82 Gauss exists 0.875 cm past the limit of the coil: a distance greater than the MCP or detector's spacing from the coil's boundary.

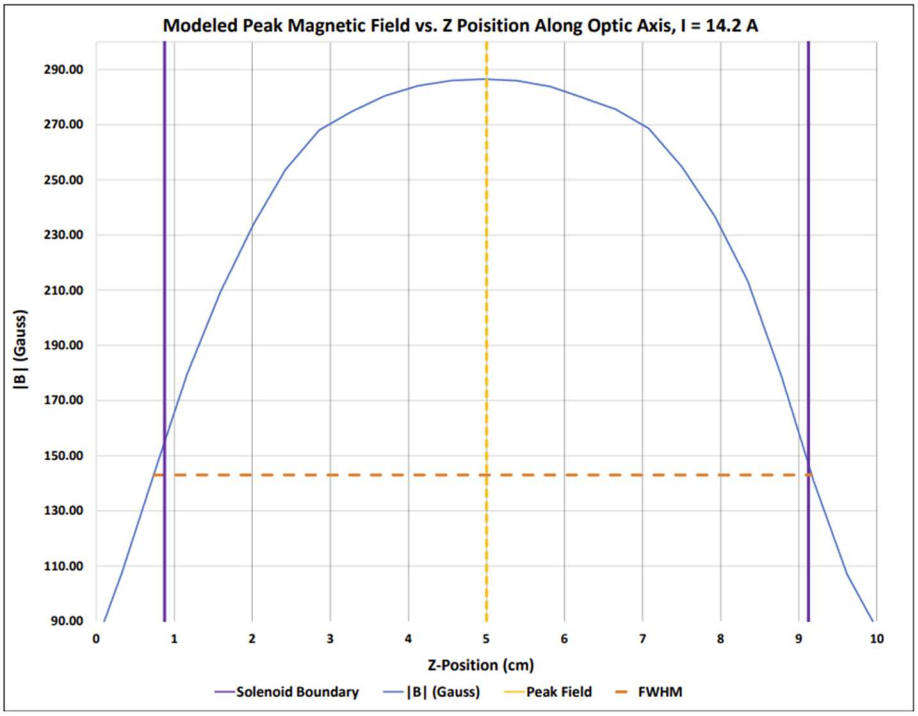

Figure 7: Modeled peak magnetic field magnitude along the optic axis.

The radial magnetic field profile is modeled along various lengths of the solenoid. Figure 8 shows the radial field magnitude inside the bounds of the solenoid at the following z-positions: the coil's center, boundary, and halfway in-between. In the center of the coil there is a near-constant field magnitude of 286 Gauss, with a slight increase of 2.6 Gauss approaching the radial boundary of the coil. At the edge of the solenoid, there is a lower field magnitude of 146 Gauss, with an increase of 22.1 Gauss over the radial boundary. At the midpoint of the coil, the average field magnitude is 93.7% the magnitude of the peak field, with an overall magnitude of 268 Gauss. The field magnitude at the midpoint increases radially by 8 Gauss. Overall, Z-distances farther away from the center of the coil have more variability in their radial field distribution. This can be explained by the fact that at a given Z-position, the number of turns on each side of

this point may not be equal. Thus, the radial field distribution at center of the coil is uniform whereas the end of the coil has more variability in its field magnitude.

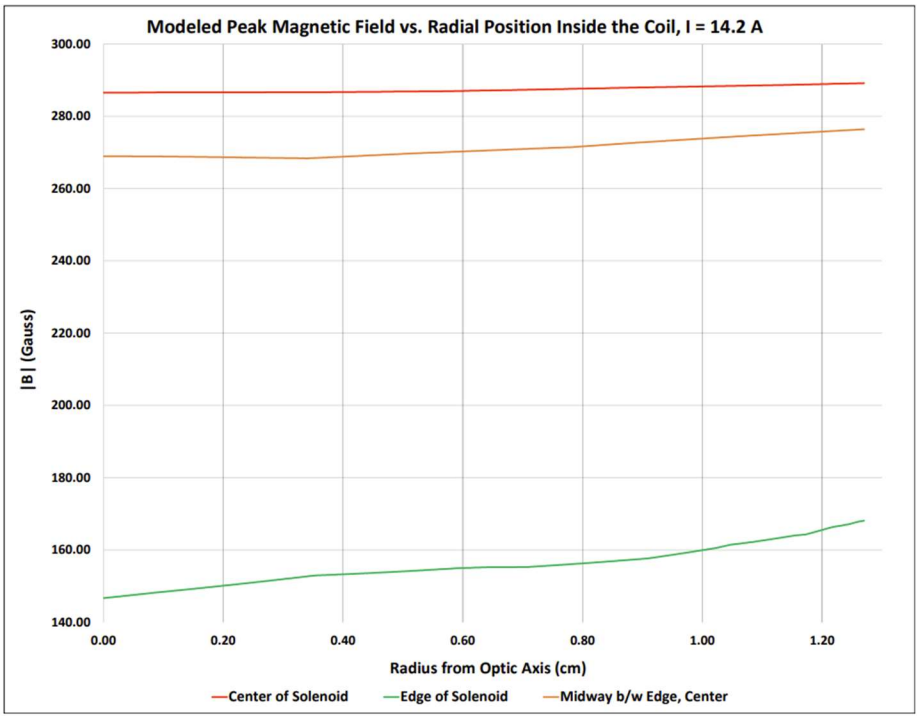

Figure 8: Modeled peak radial magnetic field magnitude inside the coil.

2.3: Electron-Trajectory Modeling

2.3.1: Program Overview

Using the programming language Python, a model was developed which simulates electron trajectories inside of the fabricated solenoid. Specifically, the model analyzes the final position of electrons at the XY plane of the electron detector. In the model, the input to the solenoid is the output of a single MCP pore. The primary goal of the model was to verify that all electrons exiting an MCP pore will be guided to the imager. In addition, another goal was to examine the estimated size of a single MCP pore's charge cloud at the plane of the electron detector. A smaller charge cloud yields less overlap across MCP pores and thus reduces the

amount of distortion between the input signal to the MCP and the final electron image at the detector.

Python was used because of the existing library Magpylib [8], an open-source Python library developed for complex magnetics problems. Python is also capable of solving differential equations at high speeds. Magpylib has built-in commands capable of calculating magnetic field magnitudes in 3-dimensions. The simulation was developed with a high-level language due to the complete freedom to customize and set any desired simulation parameters. The script is a high-electron count, single-pore model that calculates the trajectories of electrons in the drift field of the solenoid, specifically tracking the electrons' intersection with the imaging plane. The Python code discussed in the following section can be found in Appendix C.

2.3.2: Simulation Setup

The solenoid and its parameters are imported to the model, as displayed in Figure 9. With this information, Python is used to calculate the magnetic field magnitude at any point within the model. 10,000 electrons are given initial positions at the center of the input side of the solenoid, located at (0, 0) in the XY object plane. The electron origin point reflects the center of an MCP pore's output, which is also along the optic axis. Each electron is given an initial velocity and angle which are sampled from their own statistical distributions. The initial electron energies and angles from Figure 2 were traced, reproduced as statistical distributions, and implemented in Python, as shown in Figure 10. The distributions from Figure 10 were sampled and used as initial condition data in the simulation. Additional information about the model's setup and the statistical distributions can be found in Appendix D.

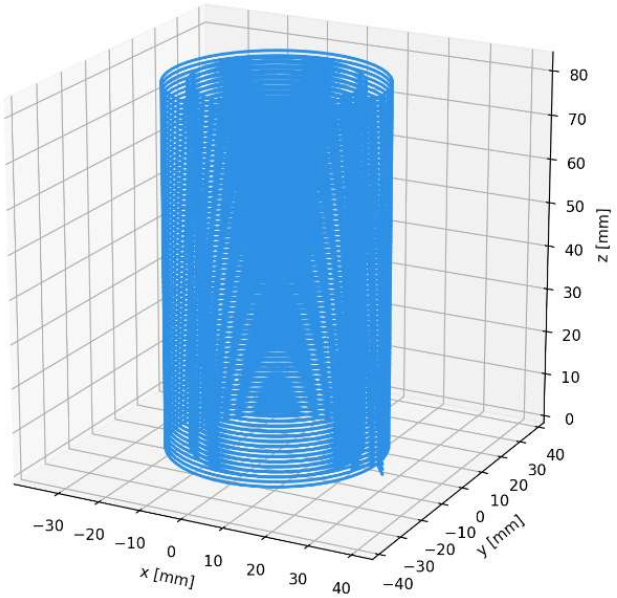

Figure 9: Solenoid displayed in the Python model.

The following differential equations [5], governing electron motion in a uniform magnetic field, are solved by Python. The solutions to the differential equations reveal the electron positions over time through the drift region. The XY positions of electron hits at the imaging plane are saved in Python and are further analyzed. Statistics about the electron positions at the imager are calculated, and different representations of the final image are created for further analysis.

$$m_e \frac{d^2x}{dt^2} = e(B_y \frac{dz}{dt} - B_z \frac{dy}{dt})$$

$$m_e \frac{d^2y}{dt^2} = e(B_z \frac{dx}{dt} - B_x \frac{dz}{dt})$$

$$m_e \frac{d^2z}{dt^2} = e(B_x \frac{dy}{dt} - B_y \frac{dx}{dt})$$

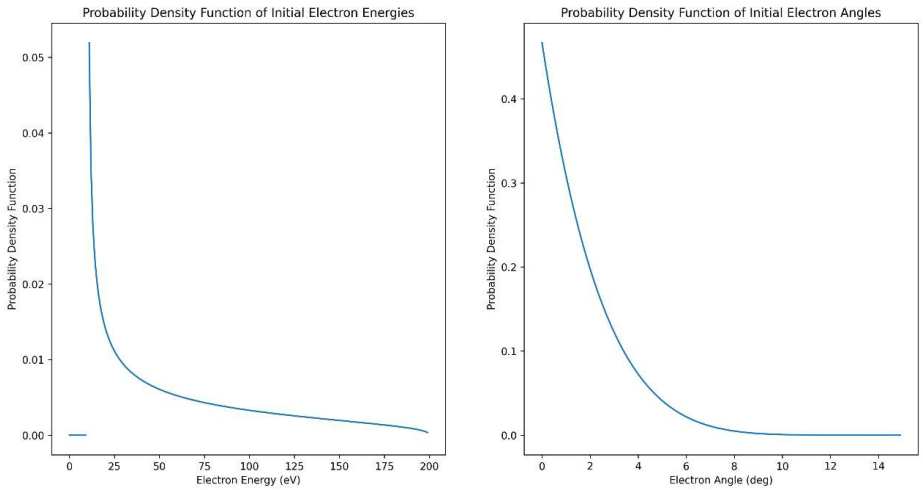

Figure 10: Reproduced beta distributions of initial electron energy and angle.

2.3.3: Simulation Results

The initial conditions sampled from the distributions in Figure 10 are displayed in Figure 11, as used in the simulation. It is noteworthy that each electron's trajectory is directly influenced by its initial velocity and angle upon exiting the MCP pore, as suggested from the differential equations governing electron motion.

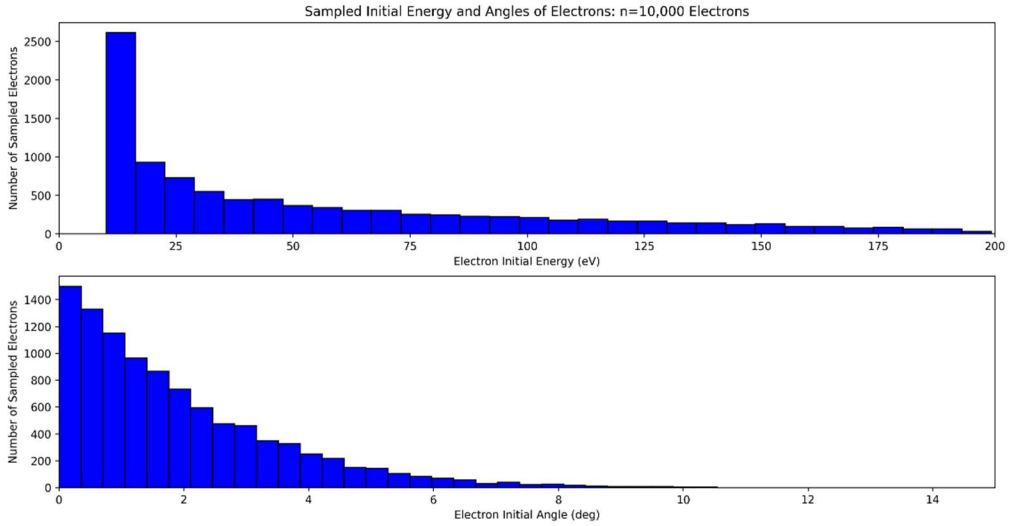

Figure 11: Sampled electron initial energy and angles for n=10,000 electron model.

Electrons hits are analyzed at the XY plane of the electron detector, located at the end of the coil lengthwise. The metric used to quantify electron positions at the imaging plane is the radius from their initial position (0, 0) to their final position (X, Y) within the XY plane. Figure 12 gives a visual representation of the final electron image at the detector. As shown in Figure 12, the distribution of modeled electron hits at the detector is Gaussian. Within the XY plane, the highest count of electrons is centered around their origin (0, 0) within the plane, with the number of hits decreasing radially.

Statistics of the electron radii were run, resulting in an average radius of 54.0 μm and a standard deviation of 69.4 μm. The smallest and largest electron radii are 0.058 μm and 824.75 μm, respectively. Due to the low angles of the sampled initial angle distribution, there is a higher frequency of electrons with radii less than 100 μm, denoted by green dots in Figure 12. At the imaging plane, 83.8% of electrons had radii less than 100 μm. These electrons travel closer to the optic axis, causing uniform motion along the axis towards the imaging plane. In addition, 11.5% of electrons from the simulation had radii in between 100-200 μm. However, as some electrons exit the channel pore with both higher energies and larger angles, their resultant radii increase. While the larger radii at the imaging plane may cause distortion of the electron-image, the results from Figure 13 suggest an exponential decrease in the number of electron hits with increasing radii. The model resulted in a mere 4.7% of electrons with radii greater than 300 μm.

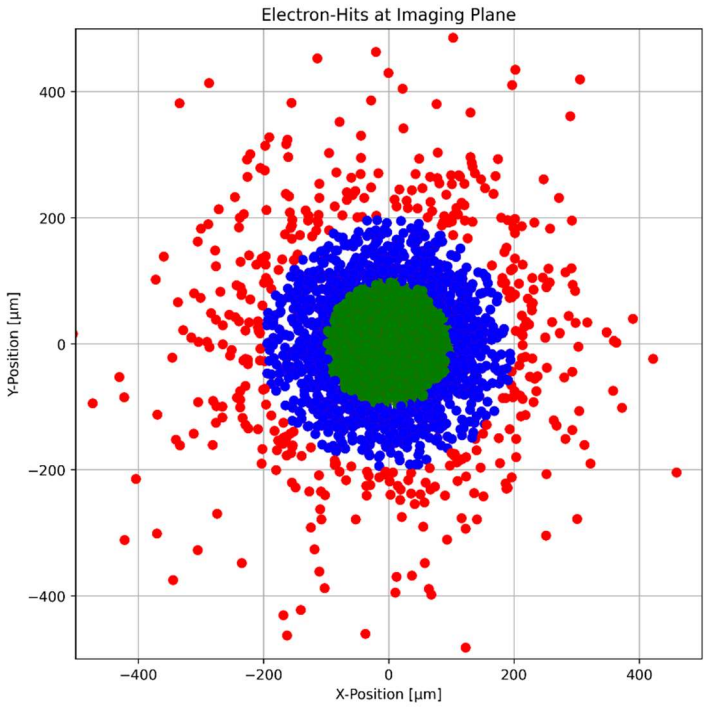

Figure 12: Electron hits at the imaging plane

(Green: radius below 100 µm, Blue: radius between 100-200 µm, Red: 200 µm or larger).

Ultimately, the goal of validating that the fabricated solenoid can guide all electrons exiting an MCP pore to the electron detector is achieved. In addition, the model suggests that the field created by the solenoid limits the size of an MCP output charge cloud to a tolerable value, where the average radius of an electron trajectory is below 100 µm. While the electron trajectory model only simulates a single pore of the MCP, it still gives useful insight into the expected size of a single pore's output charge cloud at the detector. The electric field caused by the high-voltage bias between the MCP and imager is not considered in the model; however, this large potential difference serves as an accelerating field. Therefore, the field will decrease the radius of electron trajectories and reduce the amount of overlap in separate output charge clouds. Another shortcoming of the model is that electron-electron repulsion is not implemented.

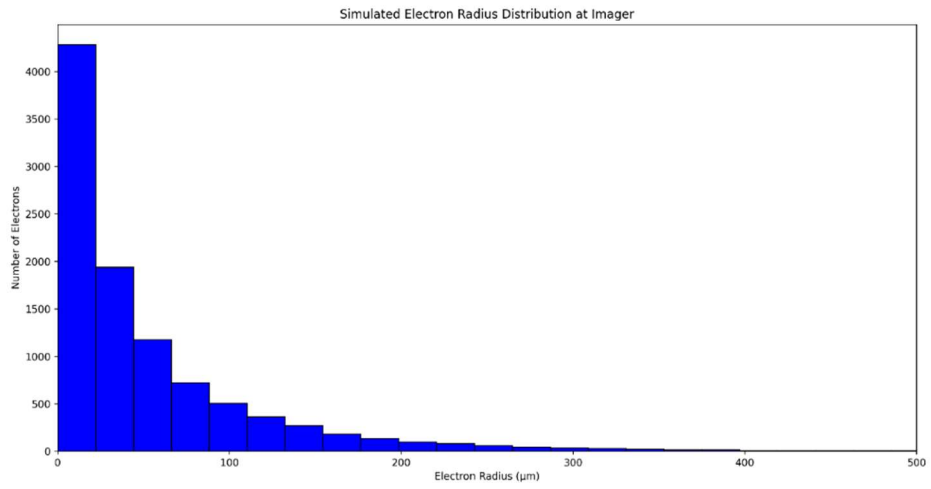

Figure 13: Histogram of modeled electron radii from n=10,000 electrons.

2.4: High-Current Pulser Circuit Design

A significant challenge in generating high fields with a solenoid is the ability to produce and sustain high current. Due to the limited power delivery of benchtop power supplies, a custom circuit was designed to deliver the target current of 12.5 A, as shown in Figure 14. To ensure that the coil's wire doesn't get damaged by the high temperatures associated with DC current in-vacuum, a current pulsing method was chosen.

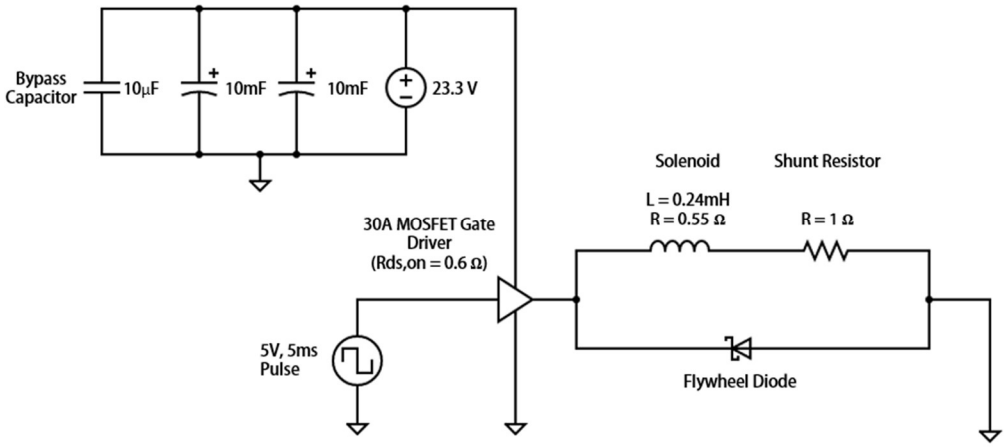

Figure 14: Designed solenoid pulser circuit diagram.

The pulser circuit is based around using a low-side power MOSFET gate driver which serves as the switch from a large capacitor bank to the load. The device chosen is an IXYS IXDN630 gate driver, chosen due to its high current carrying capacity of 30 A, quick response time of 20 ns, and relatively high voltage rating of 40 V. A schematic of the gate driver is shown in Figure 15. The gate driver is a buffer with low output impedance, whose PMOS is on as long the supply voltage is greater than the under-voltage lockout (UVLO) of 12.5 V and the input signal (IN) is greater than 0.8 V. The PMOS built-in to the gate driver has an on-channel resistance (Rds,on) of 0.6 Ω, contributing to the overall resistance of the circuit.

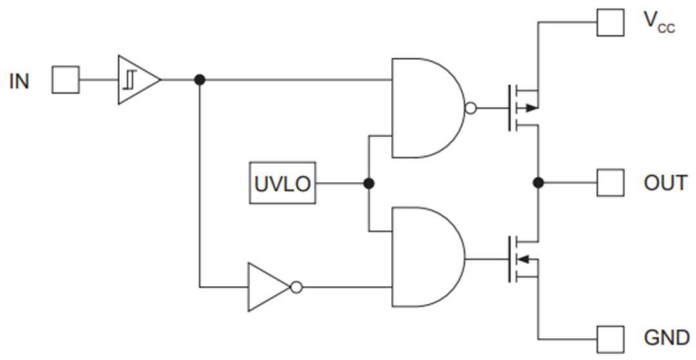

Figure 15: IXYS IXDN630 MOSFET gate driver schematic.

When the gate driver receives a high signal at the input pin, the capacitors have a closed path to ground and will consequently start to discharge. Current flows through the PMOS of the gate driver and to the output pin of the gate driver. The output pin of the gate driver is connected to the load: the coil connected in series with a shunt resistor. While the shunt resistor decreases the current through the coil, it significantly extends the RC time constant of the circuit, slowing down the rate at which the capacitors discharge. In addition, since the shunt resistor is 1 Ω, the current through the coil can be measured by probing the voltage across the shunt. There is a reverse biased Schottky diode with a large forward drop that is connected in parallel with the

load, serving as a flyback diode. The pulsing circuit was first prototyped, and a PCB was later designed, built, and tested. Appendix E gives more information about the designed PCB along with the specific electrical components used in the circuit.

2.5: LTSpice Pulser Circuit Modeling

2.5.1: Program Overview

The pulsing circuit is modeled using LTSpice circuit simulation software. The circuit was modeled to validate the functionality of the concepted circuit, aimed at verifying whether achieving the target current of 12.5 A is plausible. Since 12.5 A is an extremely large and hazardous current, circuit modeling enables safe prototyping through simulation. LTSpice was chosen since the numerical methods that the software uses yield sufficiently accurate predictions to real-life circuitry. In addition, it was chosen because it is open-source software with an abundance of available documentation [9]. Each component's properties in the simulation can be modified to include non-ideal properties that real electrical components possess, such as parasitic resistances, capacitances, and inductances, allowing for a more realistic circuit model.

2.5.2: Simulation Setup

Figure 16 displays the equivalent circuit model used in the simulation. Equivalent circuit models of components like the MOSFET gate driver and benchtop power supply were used to ensure an accurate simulation that matches the real-life measured behavior of the circuit. Further information about the simulation setup can be found in Appendix F. For simplicity, the MOSFET gate driver is modeled by two voltage-controlled switches with Rds,on and Rds,off values taken from the datasheet. The circuit is simulated over 10ms, with a pulsed 5 V, 10 ms square-wave input signal.

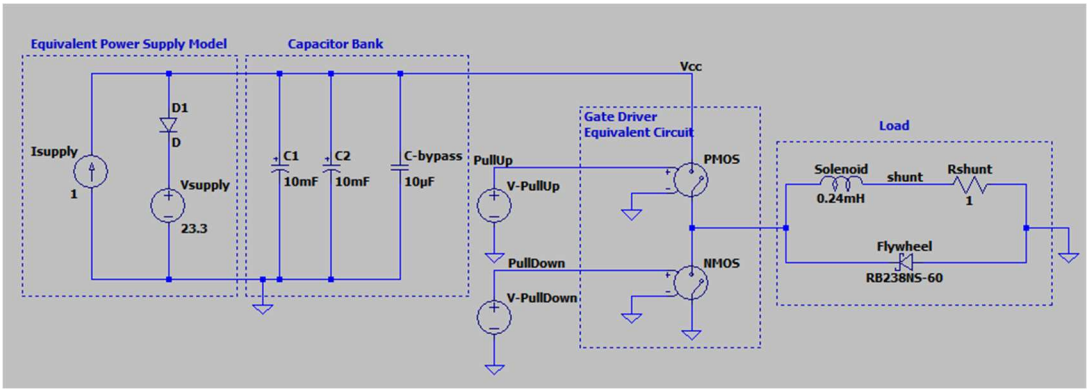

Figure 16: LTSpice equivalent circuit schematic of solenoid pulser circuit.

2.5.3: Simulation Results

The simulation was run given the parameters in section 2.5.2 and the solenoid current was examined. Figure 17 shows the current profile flowing through the solenoid over time. A peak current of 11.1 A is reached 0.67 ms after the input signal is asserted high. After the peak current is reached, there is a near-linear decrease in the magnitude of the current from 11.1 A to 9.14 A over 9.33 ms. Once the input signal is asserted low, the gate driver's PMOS turns off, effectively removing a path from the capacitor bank to ground. When this occurs, there is an abrupt decrease in the amount of current flowing through the coil, causing a negative voltage spike across the inductor: the flyback diode connected in parallel with the coil quickly dissipates the energy stored in the coil's magnetic field.

The results of the simulation suggest that at a supply voltage of 23.3 V, the pulsing circuit will not be able to produce the target current of 12.5 A; however, the measured profile has a peak current of 14.2 A. This discrepancy is likely a result of the capacitor bank being charged to a value greater than 23.3V. Since an extremely high-capacitance capacitor bank is connected in parallel with the power supply, the moment the supply is abruptly turned on, the capacitors strongly resist the abrupt change in voltage. There is likely a large surge in power from the power

supply in response, which could result in the supply voltage of 23.3 V being exceeded and additional energy being stored in the capacitors. Additional LTSpice modeling suggests that a supply voltage of 27.1 V yields the measured current of 14.2 A: an additional 3.8 V being output by the power supply during a transient is certainly feasible.

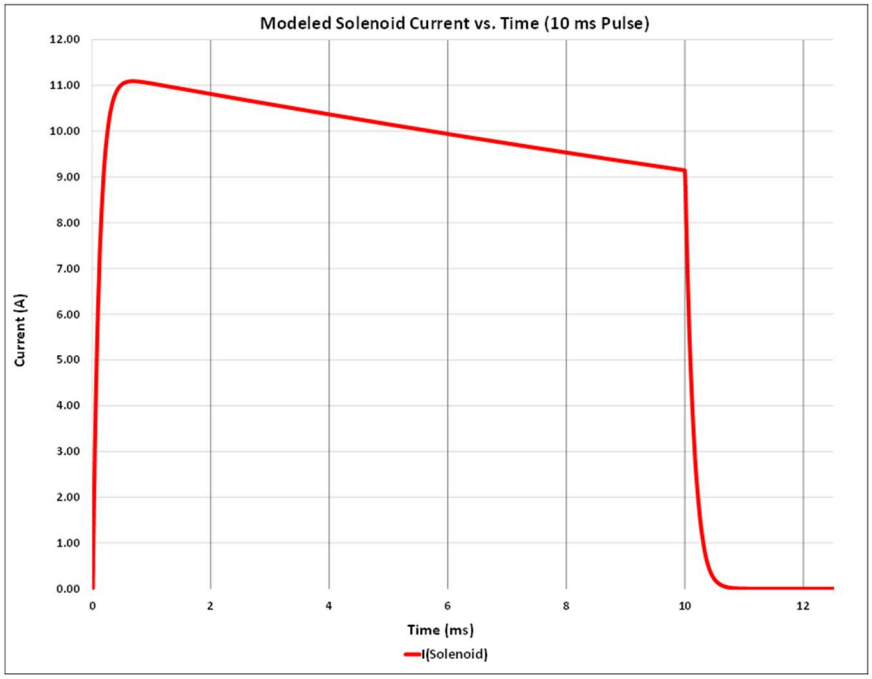

Figure 17: LTSpice simulated solenoid current, 10 ms pulse.

The large 10 mF capacitors in parallel with the power supply cause a drop in the supply voltage as they discharge. The drop in supply voltage is monitored to ensure that it never drops below the UVLO of 12.5 V, which would remove the PMOS' path to ground. Based on the results in Figure 18, the supply voltage drops from 24.1 V to 19.6 V, suggesting that the gate driver will not pull down while the input signal is high, and the gate driver will function as desired.

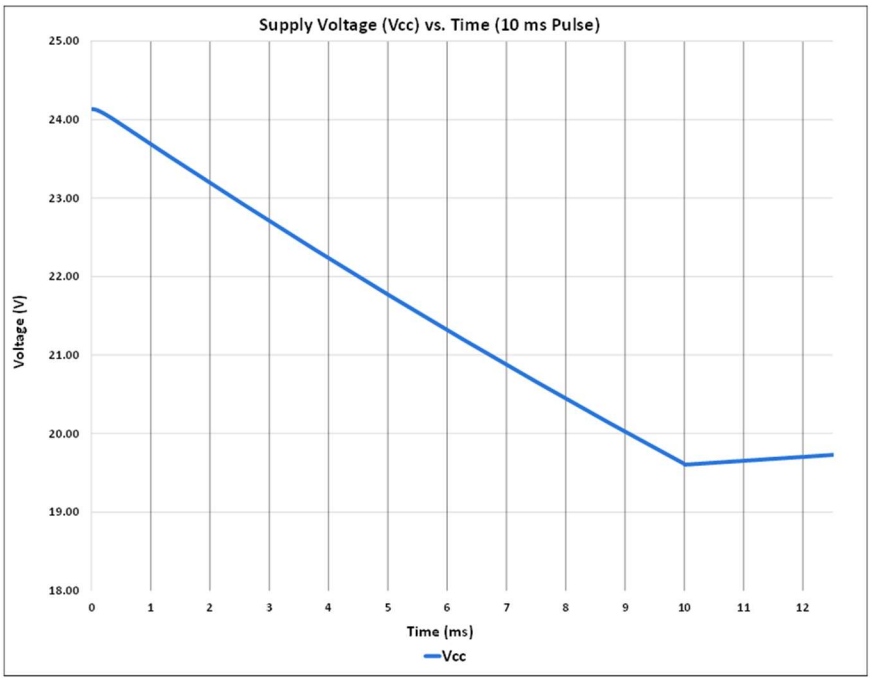

Figure 18: LTSpice simulated drop in supply voltage, 10 ms pulse.

Chapter 3

3.1: Pulsing Circuit Measurements

The pulsing circuit was assembled, tested, and connected to the solenoid. As presented in Table 2, the supply voltage was swept from 15 V to 27.5 V, receiving 5 V, 5-ms square-wave input pulses from a signal generator. The current through the solenoid was measured by probing the voltage across the series 1-ohm shunt. A peak current of 17.1 A was measured through the solenoid at the maximum supply voltage of 27.5 V.

Supply Voltage (V)	Peak Current (A)	Minimum Current (A)
15	8.9	7.5
18	11.0	9.2
20	12.3	10.1
22.5	14.1	11.7
25	15.6	12.9
27.5	17.1	14.4

Table 2: Measured solenoid current, 5-ms pulse length.

After connecting the solenoid to the vacuum-feedthrough pins, supply voltages above 25 V yielded high-noise current profiles with an RMS current of approximately 5 A, a direct result of the added inductance from the vacuum feedthrough pins. At higher supply voltages, the noise profile was accentuated due to the greater amount of stored energy. To suppress the noise profile, the supply voltage was decreased to the highest possible stable value of 23.3 V, as lowering the supply voltage decreases the amount of inductive ringing. The current profile at a supply voltage of 23.3 V is shown in Figure 19. A measured peak current of 14.2 A was measured with a minimum current of 9.8 A over a 10-ms pulse length, which was extended by 5-ms due to the 2.9 A loss in peak current from the vacuum feedthrough connection.

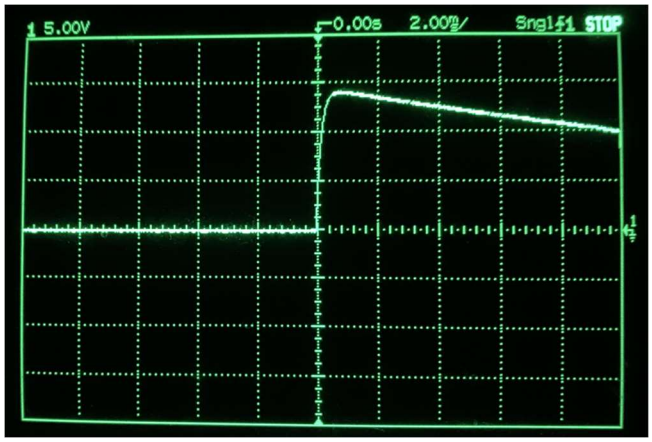

Figure 19: Pulsed current waveform, 10-ms pulse length at Vcc = 23.3 V.

3.2: Field Measurements

Using a Lakeshore Model 475 DSP gaussmeter and 400-series hall probe, the magnetic field profile of the solenoid was measured. The hall probe was positioned at precise locations inside of the coil enclosure while the solenoid was pulsed by the circuitry at a supply voltage of 27.5 V and a peak current of 17.1 A. Since the magnetic field measurements were taken before the supply voltage and peak current were reduced to 23.3 V and 14.2 A, the field measurements are scaled by 0.83 to reflect the in-vacuum conditions.

The peak field was measured along the optic axis of the coil, shown in Figure 20. A peak magnetic field magnitude of 285.2 Gauss was measured at the center of the optic axis. The measured field profile was interpolated to calculate a full width at half maximum of 8.4 cm: 0.2 cm longer than the physical bounds of the coil. The radial peak field profile was also measured along three different positions of the coil lengthwise: the center, the edge, and the midpoint in between. Along each of these lengths of the coil, the field was measured at the radial center, the coil's radial boundary, and the midpoint in between. The measured field profile is given in Figure

21, with a resulting peak field of 288.1 Gauss at the center of the coil lengthwise and at the radial boundary of the coil.

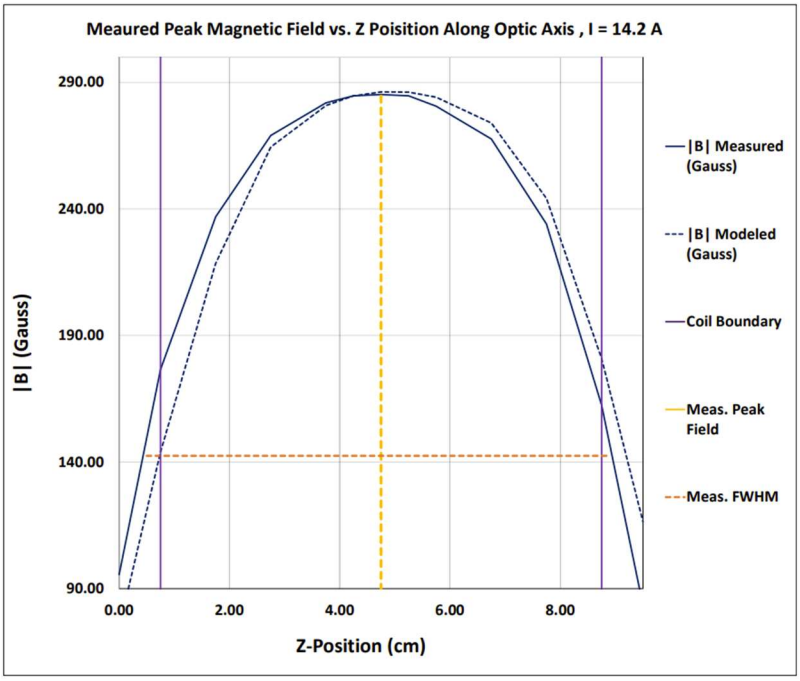

Figure 20: Measured peak magnetic field profile along the optic axis.

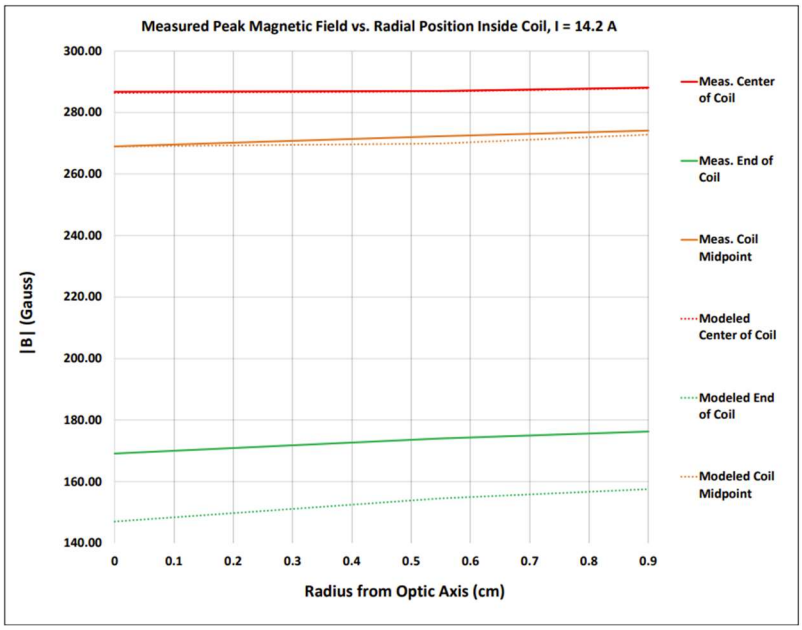

Figure 21: Radial profile of the measured peak magnetic field.

3.3: Microchannel Plate Electron-Imaging

3.3.1: Experimental Setup

The solenoid's ability to condense MCP output electrons into an electron beam is experimentally verified. Figure 22 presents the experimental setup which is implemented under UHV. The input electron source is a thermionic emitter, whose cathode is coated in barium oxide and biased at -7 kV. The input electron beam is focused onto the input side of the MCP by modulating the extracting and focusing potentials built-in to the electron source. Fixed biases of +2 kV and +2.2 kV are applied to the input and output sides of the MCP, respectively. The biases of the accelerating grid and phosphor plate are variable, as listed in Table 3.

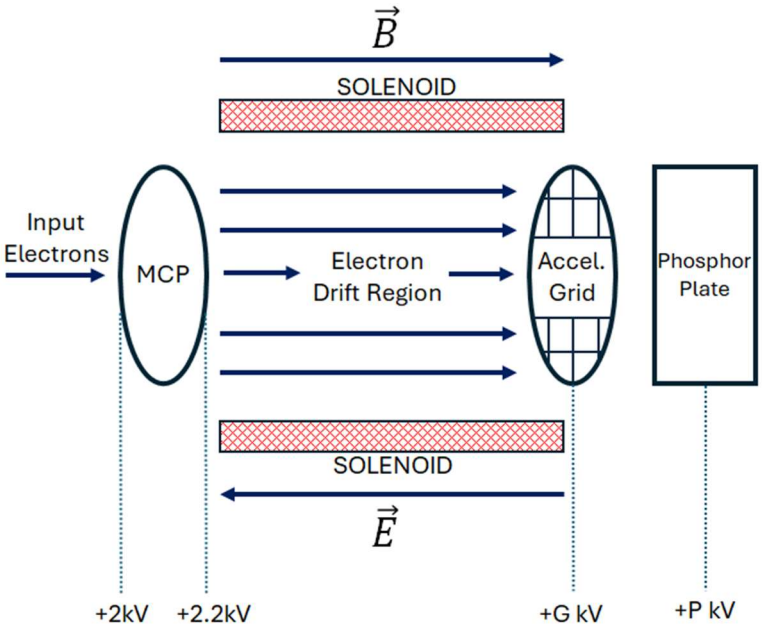

Figure 22: Experimental setup.

For each of the test biases outlined in Table 3 the solenoid was pulsed for 10-ms. The current profile for each pulse is represented in Figure 19, with a peak current of 14.2 A. Over the

duration of the pulse, the phosphor plate was recorded through a transparent vacuum window at 1080p and 24 FPS. One frame per recorded video captures the beam condensing as the solenoid is pulsed. Three different shots were taken for each test bias after the capacitors in the pulsing circuit were fully discharged.

Test Bias	V_{grid} (kV)	$V_{phosphor}$ (kV)
1	3.5	3.5
2	3	3
3	3.5	3
4	4	3.5
5	4	2
6	3	2.5
7	4.5	4

Table 3: Experimental test biases.

3.3.2: Raw Intensity and Image Background Results

Figure 23 shows the static background and pulsed beam profiles of the phosphor plate under test bias 1. The background and beam profiles of each test bias vary in shape, intensity, and centering due to the varying potentials on the grid and imaging plate. All unedited phosphor plate images can be found in Appendix G.

Using ImageJ image processing software, the intensity statistics of the background and beam profiles for each test bias are generated. Statistics of the phosphor plate intensity are calculated inside of the PEEK ring, which bounds the drift region. The raw intensity values, summarized in Table 4, are normalized by the largest intensity value that was observed. The highest intensity beams are captured under test biases 1, 4, and 7, which consequently exhibit the highest intensity background profiles and thus the lowest peak beam-to-background intensity ratios. Conversely, the low intensity beams from test biases 5 and 6 have some of the highest

average beam-to-background intensity ratios of 2.3 and 15.0, suggesting that grid and phosphor biases under +3kV extract very little signal without the assistance of the external magnetic field.

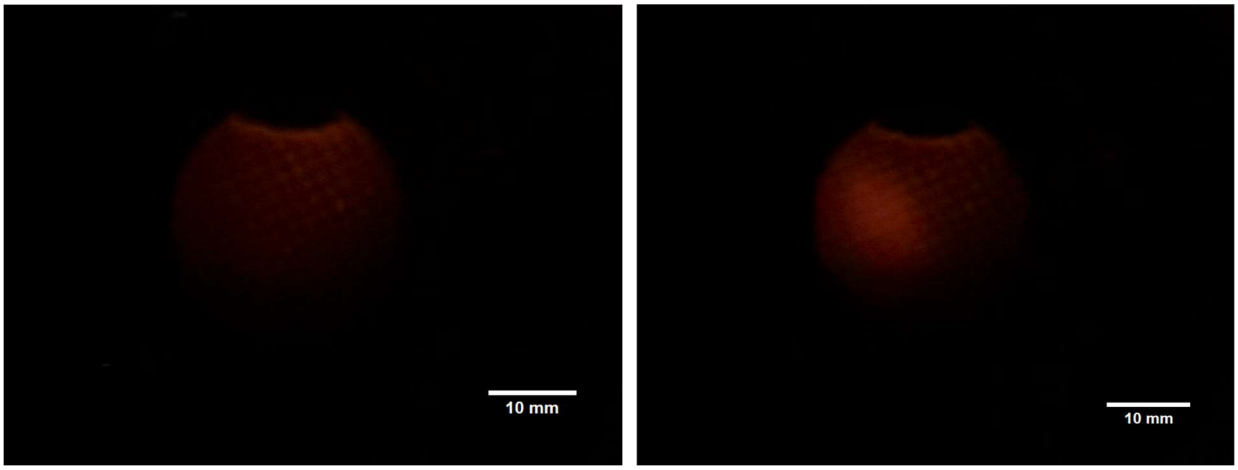

Figure 23: Test bias 1 phosphor plate image of: (a) background profile (b) pulsed beam profile.

Test Bias	Peak Background Intensity	Peak Beam Intensity	Peak Beam/ Background Ratio	Average Background Intensity	Average Beam Intensity	Average Beam/Background Ratio	Standard Deviation (mm)
1	0.386	0.504	1.31	0.101	0.146	1.62	10.19
2	0.119	0.237	1.99	0.020	0.063	3.15	5.51
3	0.248	0.336	1.35	0.056	0.094	1.68	6.88
4	0.386	0.643	1.67	0.141	0.201	1.42	13.03
5	0.039	0.079	2.02	0.009	0.021	2.33	1.90
6	0.020	0.079	3.95	0.002	0.030	15.00	2.28
7	0.792	1	1.26	0.221	0.310	1.40	19.75

Table 4: Statistics of raw background and beam intensities.

3.3.3: Background Subtracted Beam Intensity Profiles

The additive background subtraction feature in ImageJ was utilized to isolate and accentuate the electron beam formed by the solenoid while simultaneously suppressing the beam's background profile, enabling the analysis of the isolated beam shaped by the solenoid. The consistent background profile is an artifact of the accelerating grid, as seen in Figure 23. During the experiment the input electron source was constantly on, meaning that the MCP was amplifying

the input electron signal even while there was no magnetic field. Figure 23 demonstrates how background subtraction can highlight the solenoid's role in shaping the electron beam on the phosphor imaging plate.

The background subtracted intensity profiles are displayed in Figure 24, whose Gaussian intensity profiles are indicative of a clearly defined electron beam. The varying magnitude of beam intensities across different test biases is a direct result of the varying magnitude and ratio of the high-voltage grid and phosphor plate biases. Via ImageJ, each of the distributions were assigned a Gaussian fit, with heights forced to zero, as shown in Figure 25. The fit Gaussian distributions are of the form:

$$I = (b - a) * \exp\left(-\frac{(x - c)^2}{2d^2}\right)$$

The statistics of the Gaussian fits are summarized in Table 5 and the respective parameters for each fit can be found in Appendix H. Notably, the high intensity beams labeled in Figure 24 all have grid and phosphor potentials of at least +3.5 kV. The background subtracted intensity profiles show improvement over the raw intensity data, highlighted by the large difference in standard deviations between Tables 4 and 5. Whereas the high intensity beams have an average standard deviation of 14.3 mm for their raw intensity values, the background subtracted images have an average standard deviation of 3.1 mm. This suggests that a large amount of the signal in the raw high intensity images is an artifact of the high-intensity background image on the phosphor plate. For reference, the average standard deviation across moderate intensity beams was 2.4 mm for the raw intensity images and 3.0 mm with background subtraction.

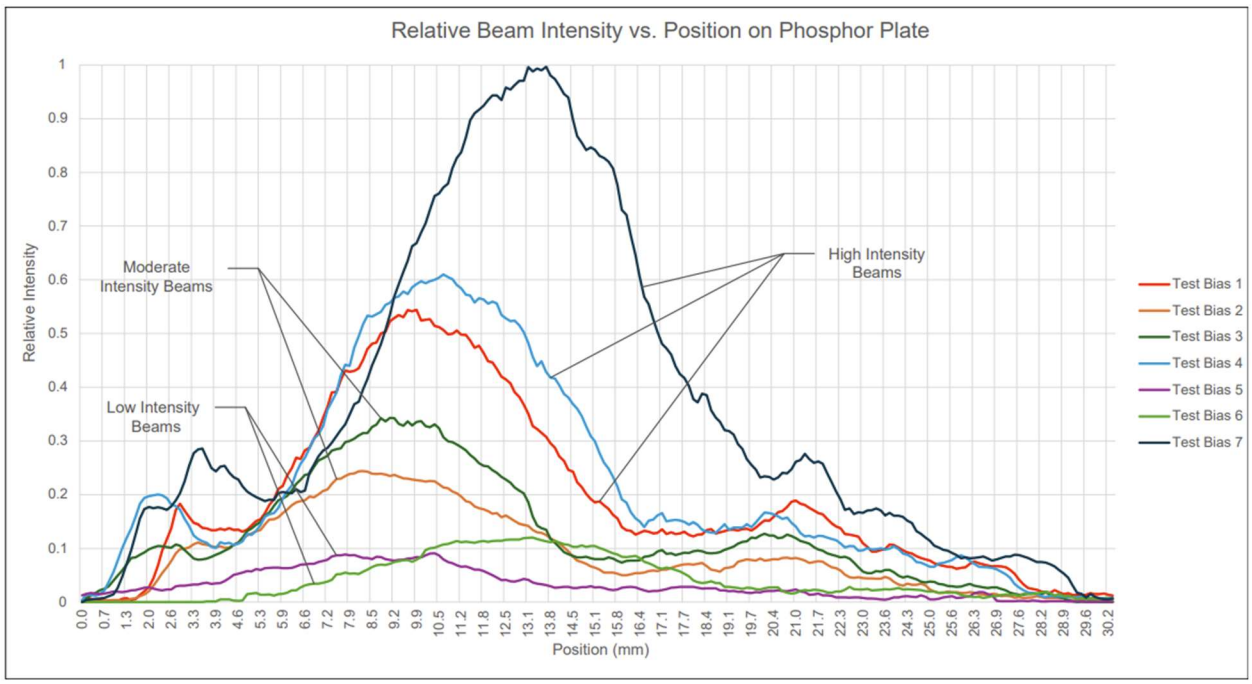

Figure 24: Background subtracted beam intensity profiles.

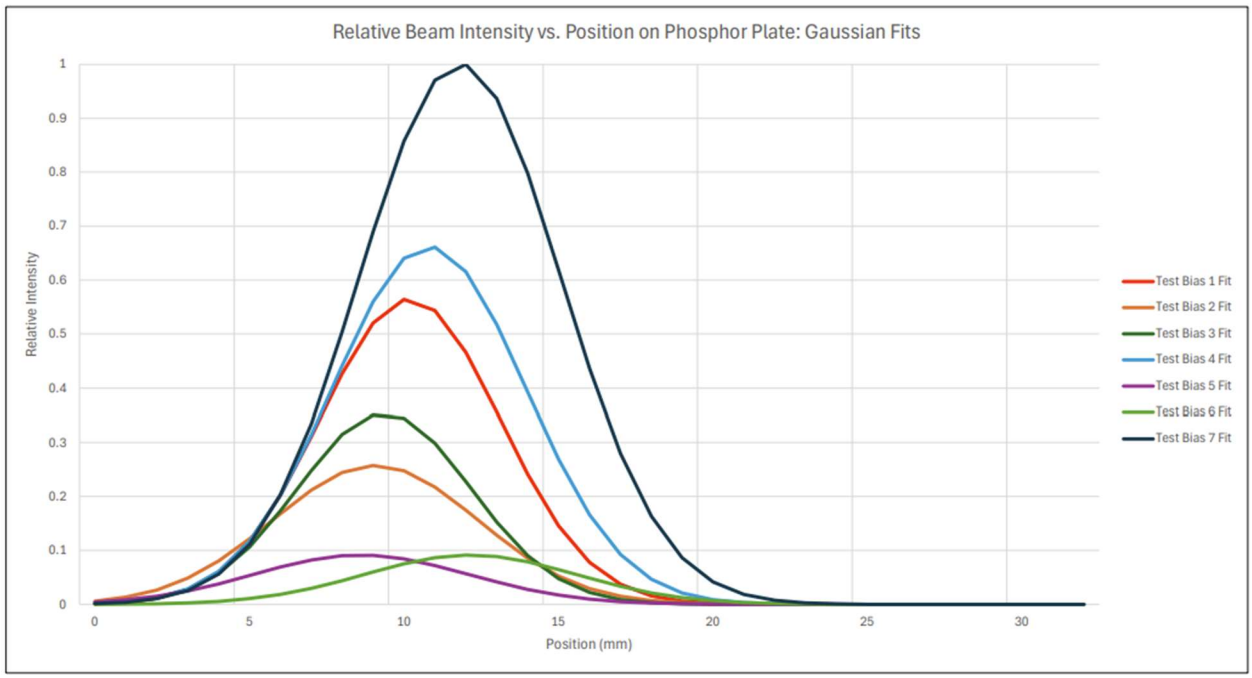

Figure 25: Background subtracted beam intensity Gaussian fits.

Test Bias	Relative Peak Intensity	Standard Deviation (mm)	FWHM (mm)	R^2
1	0.56	2.92	8.7	0.927
2	0.25	3.32	9.8	0.909
3	0.36	2.81	8.8	0.908
4	0.65	3.12	9.1	0.947
5	0.09	3.49	10.3	0.938
6	0.08	3.43	12.8	0.969
7	1	3.25	9.8	0.979

Table 5: Summary of background subtracted intensity Gaussian fits.

3.3.4: Thresholded Beam Intensity Profiles

The beam intensities formed on the phosphor plate are filtered with ImageJ to remove the background profile present when the solenoid is off. Only the lower intensities that constitute the background profile were filtered. Removing the lower intensities from the static background profile enables the isolated analysis of the high intensity portions of the beam, where the solenoid's influence is most evident. Intensity thresholding enables the characterization of the beam's relative spot size, shape, and centering within the intensity range defined by the user. The process of intensity filtering is illustrated in Figure 26, with varying lower thresholds and an upper threshold of the maximum intensity. Once a threshold is applied to an image and the filtered intensities are selected, an ellipse is fit to the selected area. Each ellipse is analyzed to determine the beam area, centering, rotation, and the average intensity within the selected threshold.

The results of the fitted ellipses are summarized in Table 6. Each test bias has a lower limit of one standard deviation above its respective mean intensity and an upper limit of the maximum possible intensity. This lower threshold was chosen due to the skewed beam profile in Figure 26(a), where too low of a threshold results in hits from the background profile being selected, opposed to the actual beam created by the solenoid. The average intensity metric in

Table 6 applies solely to the thresholded area: a measure of the true thresholded intensity per unit area without lower intensities skewing the average.

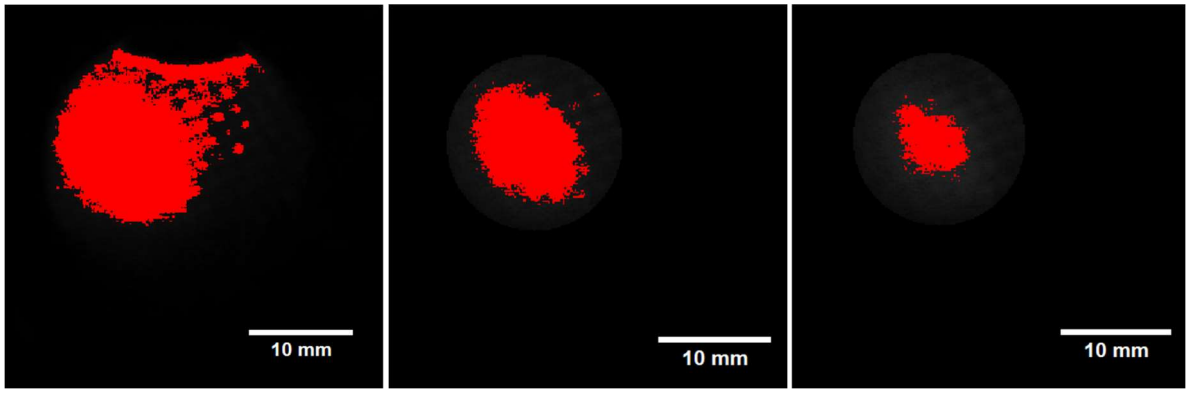

Figure 26: Test bias 1 intensity thresholding, lower limit: (a) mean intensity (b) mean intensity + 1 standard deviation (c) mean intensity + 2 standard deviations.

Test Bias	Beam Area (mm^2)	Rel. Average Intensity	Beam Center to Origin Dist. (mm)	Ellipse Ratio (Major/Minor)	Beam Rotation (°)
1	74.16	0.32	5.03	0.73	131.1
2	107.20	0.14	5.99	0.72	134.6
3	79.39	0.21	5.81	0.80	128.8
4	73.71	0.43	2.94	0.76	134.2
5	94.54	0.05	4.64	0.84	114.5
6	78.52	0.06	4.60	0.74	135.2
7	68.66	0.66	1.69	0.84	135.1

Table 6: Fitted ellipse summary, lower limit: test bias mean intensity + 1 standard deviation.

The fitted beam ellipses were plotted using AutoCAD software to visualize and overlay the ellipses from Table 6. Figure 27 gives a visual representation of the relative sizes and overall shapes of the beams, with lower thresholds of one and two standard deviations above each sample's average intensity. On average, the high intensity beams are the best centered, with an average offset of 3.2 mm. The moderate intensity beams are the most offset from the center, with an average offset of 5.9 mm. However, these beams have the largest average beam area of 93.3 mm^2. The low intensity beams are the most circular, with an average ellipse ratio of 0.79;

however, their relative average intensity of 0.055 is extremely low. Overall, the beams are rotated at an average of 130.5°, with little variability in their rotation.

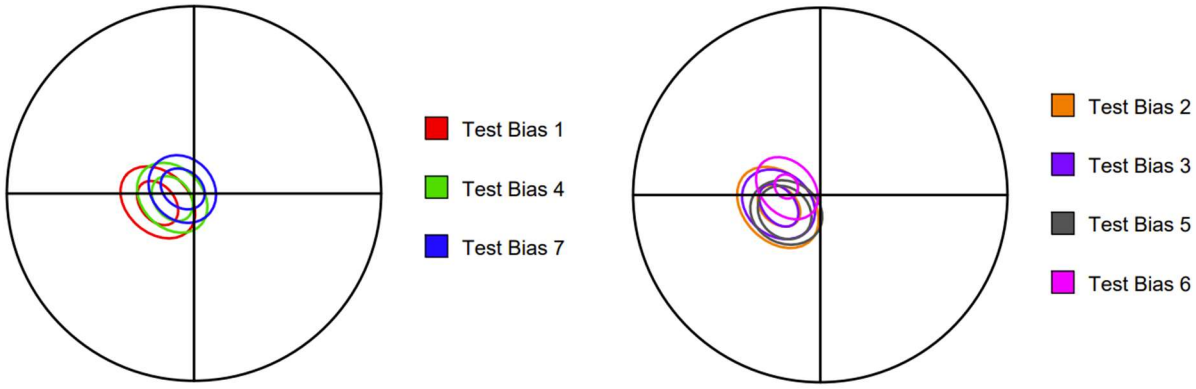

Figure 27: Plotted intensity ellipses, lower limit: mean + 1 standard deviation (outer ellipses), mean + 2 standard deviations (inner ellipses).

To further analyze the high intensity beams, a fixed threshold is set to gauge the relative beam size and shape across different test biases. Lower thresholds of 30%, 40%, and 50% of the maximum observed intensity were placed. Results of the relative beam sizes, intensities, and uniformity are summarized in Table 7 and the respective ellipses are plotted in Figure 28. Above the 50% threshold, the beam area from test bias 1 increases to a mere 0.185% of its original spot size in the 30% threshold, a consequence of test bias 1 having the lowest peak intensity out of the high-intensity shots. This highly contrasts test bias 7, which decreases to 42% of its original beam area between the 50% and 30% thresholds. Due to the high intensity of test bias 7, this bias is preferable if the goal is to get the most signal and the largest spot size to the imager. However, the beam produced from test bias 4 provides a smaller spot size with 65% of the relative intensity from test bias 7. This beam would be suitable if a high intensity per unit area beam is desired

which has a finer spot size than test bias 7, as its beam-to-background ratio of 1.67 is higher than any other high-intensity beam.

Rel. Lower Threshold	Test Bias	Beam Area (mm^2)	Rel. Average Intensity	Beam Center to Origin Dist. (mm)	Ellipse Ratio (Major/Minor)	Beam Rotation (°)
0.3	1	45.94	0.36	4.96	0.78	133.4
0.4	1	10.84	0.42	5.26	0.65	136.9
0.5	1	0.085	0.50	4.86	0.87	39.3
0.3	4	90.51	0.40	3.03	0.92	133.1
0.4	4	44.66	0.48	3.00	0.67	136.3
0.5	4	17.76	0.53	2.92	0.85	146.8
0.3	7	170.86	0.49	2.29	0.80	174.0
0.4	7	107.14	0.58	1.74	0.85	152.9
0.5	7	71.94	0.65	1.73	0.84	136.7

Table 7: Fitted ellipse summary, high intensity beams fixed thresholding.

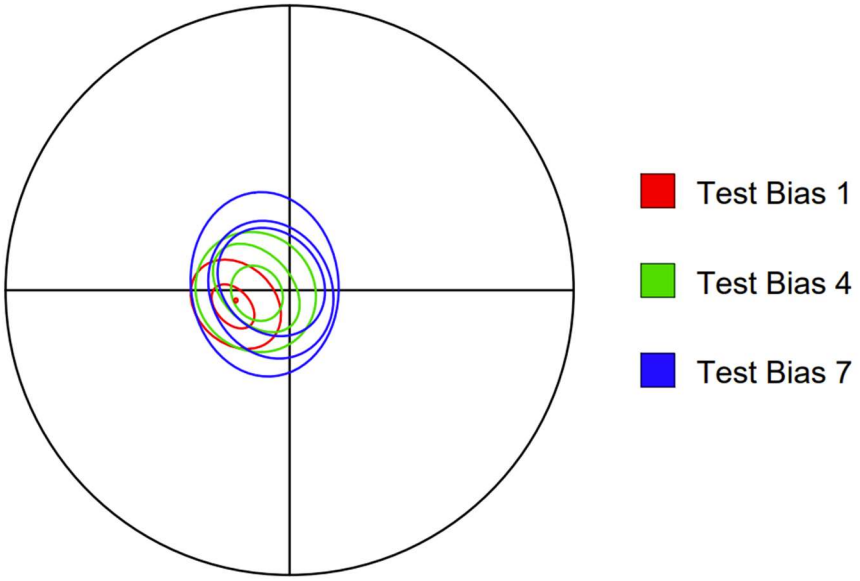

Figure 28: Plotted intensity ellipses with lower limits of: 30% (outer ellipses), 40% (middle ellipses), and 50% (inner ellipses) of maximum intensity.

Chapter 4

4.1: Conclusion

In this research, an experimental setup was formulated which guides and condenses output electrons from a microchannel plate to an electron detector. The experimental setup amplifies a weak-input electron signal into a higher intensity electron signal, as collected on a phosphor imaging plate. A solenoid and its supporting enclosure were built and tested, creating a confined area of electron drift in an ultra-high vacuum environment. The solenoid was modeled, experimentally tested, and generates a considerable magnetic field within the bounds of the drift region. The external magnetic field generated by the coil exerts a force on drifting electrons, guiding them to the imager. A magnetic field pulsing methodology was adapted, allowing the user to choose the pulse length, rate, and magnitude, provided they remain within the design's parameters. The imaging and pulsing setup can be scaled so that the solenoid creates a substantially smaller or larger magnetic field, depending on the application. The experimental setup is modular in design: various electron imagers can be substituted to measure different profiles of the electron image. In addition, the imaging setup can readily be demounted from the primary vacuum chamber and tested with different input radiation sources.

Electron imaging was performed with a phosphor screen and the coil's ability to condense electrons into an electron beam was experimentally verified. A clearly defined electron beam was reproduced on the imager, with an increase in the average light intensity by a factor of up to 15. With a fixed microchannel plate bias, different accelerating grid and imager biases were tested to find the configurations with the lowest and highest relative intensities. The overall beam shapes, intensities, and positions were analyzed under different experimental conditions. Imaging

conditions with the brightest and largest relative beam sizes were documented, analyzed, and reproduced.

Due to the poor temporal resolution of the phosphor plate and video camera used in the experimentation, the temporal response of the imaging setup was not measured. Therefore, the claim that the imaging setup is high-speed cannot be made until another electron imager is installed in place of the phosphor imaging plate. Additionally, the input electron signal was not imaged under the final imaging biases. For that reason, it is unknown whether the final image completely reflects the input electron signal, or if there is a slight aberration caused by the electromagnetic lens. While the microchannel plate, accelerating grid, and imaging plate were all biased at positive high voltage, in the future the biases will needed to be negatively offset so that the final imager is grounded. This is necessary so that the electron imager can connect to a computer to use high-speed imaging software.

The coil developed in this research enables microchannel plates to be electron-imaged with an overall reduction of the byproducts caused by the device's signal gain. The significance behind the broader imaging setup is that it can be interpolated and utilized to image different types of input radiation. Additional energy-conversion devices can be installed in tandem with the MCP due to the modularity of the enclosure. If ultra-high signal gain is desired, multiple microchannel plates can be cascaded in series. Based on the images and data collected in this research, it is evident that the solenoid increases the flux of electrons incident to the imaging plane, enabling electron imaging with higher contrast, bit depth, and signal-to-noise ratio.

4.2: Future Work

4.2.1: Imaging with an Electron-Sensitive Sensor

The phosphor imaging plate was used to validate that the solenoid condenses the output charge cloud of an MCP into an electron beam. The main issue regarding the phosphor plates is their poor temporal response. Using a high-speed, electron-sensitive sensor would enable the measure of the temporal response of the MCP. In addition, it would reflect the magnetic field forming and collapsing over the duration of the 10-ms pulse, which drastically impacts the spatial resolution of the resultant electron image. In addition, phosphor plates have poor spatial resolution. The images on the phosphor screen do not fully reflect the electrons collisions with the phosphor screen since the fluorescent light, a byproduct of cathodoluminescence, is analyzed rather than the true electron signal. Using an electron-sensitive imager would enable a more accurate measure of the true electron image incident to the imager.

4.2.2: X-Ray Imaging

In this research, the input signal to the MCP was an electron beam. Since MCPs are sensitive to other types of electromagnetic radiation, the experimental setup can be translated to image X-rays. High-speed X-ray imaging is very applicable and desirable for various applications in modern research. If an electron-sensitive sensor is implemented, X-ray imaging at high speeds will be feasible. However, additional energy conversion devices such as photocathodes may be needed to convert incident X-rays into electrons as the input signal to the MCP.

4.2.3: DC Magnetic Fields

Due to the relatively low energy of the input electron signal, pulsed high current was needed to condense the MCP output electrons. If X-rays are used as input signals, it may be possible that

the modified angle and energy distributions of the MCP output electrons greatly increase the spatial resolution of the electron image. In this case, using lower magnetic fields at a DC current may be feasible. For the high-speed imaging of an input X-ray signal, using a DC magnetic field is desirable because the magnitude of the field is constant over time. The electron images formed by the pulsed magnetic field vary slightly over time depending on the changing field strength: the use of a DC magnetic field could possibly yield a consistent background profile with a static, condensed electron beam reflecting the input signal.

Appendix A

Fabricated Solenoid Information

Details about the specific dimensions about the fabricated solenoid are given in Table A.1:

Length of Solenoid	8.25 cm
Number of Turns per Layer	72 Turns
Number of Layers	2 Layers
Total Number of Turns	144 Turns
Diameter of Layer 1	3.81 cm
Diameter of Layer 2	3.92 cm

Table A.1: Fabricated solenoid dimensions.

In addition, information regarding the properties of the wire used in the coil is given in Table A.2. The copper wire used in the coil is from Kurt J. Lesker Company, product number FTAK10010.

Wire Material	Copper
Wire Gauge	18 AWG
Conductor Diameter	1 mm
Outer Diameter	1.1 mm
Insulating Material	Kapton
Thermal Range	-269 to 260 °C
Resistivity	23 ohm/km

Table A.2: Solenoid magnet wire information.

Appendix B

FEMM Simulation Setup and Parameters

A simulation was set up with an open boundary, whose parameters are listed in Table B. The model was run with a solver precision of 1e-08, and a triangulated mesh with 9454 nodes was created.

Layers	7
Radius	13.4 cm
Horizonal Center	0
Vertical Center	2.5 cm
Edge Type	Dirichlet

Table B: Boundary parameters of FEMM model.

Appendix C

Electron Trajectory Modeling Python Code

This work was performed under the auspices of the U.S. Department of Energy by Lawrence Livermore National Laboratory under Contract DE-AC52-07NA27344.

```
import numpy as np
import magpylib as magpy
import scipy.special as sp
import matplotlib.pyplot as plt
from scipy.interpolate import interpn
from scipy.integrate import solve_ivp
from scipy.stats import beta
from scipy.stats import tstd

# Set up the solenoid as a collection of current loops
coil1 = magpy.Collection()

# size of the mesh in cm +/-
mesh_size_x = 10
mesh_size_y = 10
mesh_size_z = 100

#number of electrons
numPoints = 10000

#Length of coil in mm
coilLen = 82.5

#Number of turns PER LAYER from fabricated solenoid
```

```
numTurns = 72

#First row of turns
for z in np.linspace(0, coilLen, numTurns):
    winding = magpy.current.Loop(
        current=12.5,       # A
        diameter=38.1,      # mm
        position=(0, 0, z),
    )
    coil1.add(winding)

#Second row of turns
for z in np.linspace(0, coilLen, numTurns):
    winding = magpy.current.Loop(
        current=12.5,
        diameter=39.2,   # = Inner diameter plus the diameter of the magnet wire (1.1 mm)
        position=(0, 0, z),
    )
    coil1.add(winding)
coil1.show()

#(tsz, tsy, tsx = x, y, z (cm))
tsx = np.linspace(-mesh_size_x, mesh_size_x, 51)
tsy = np.linspace(-mesh_size_y, mesh_size_y, 51)
tsz = np.linspace(0, mesh_size_z, 101)
grid = np.array([[[(x, y, z) for x in tsx] for y in tsy] for z in tsz])
B = 10*magpy.getB(coil1, grid)     #getB is in mT, thus B(gauss)=10*B(mT)

def Bx(x,y,z):
    return interpn((tsz,tsy,tsx), B[:,:,:,0], (x,y,z))
```

```
def By(x,y,z):
    return interpn((tsz,tsy,tsx), B[:,:,:,1], (x,y,z))
def Bz(x,y,z):
    return interpn((tsz,tsy,tsx), B[:,:,:,2], (x,y,z))
#_____________________________________________________________________________
#                        ENERGY AND ANGLE DISTRIBUTION
#_____________________________________________________________________________

#ENERGY alpha/beta calculated in beta-distr script
alphaE, betaE, scaleE, locE = 0.443, 1.400, 190, 10

xrangeE = np.arange(0, 200, 1)

sampleE = [0]*numPoints

for i in range(len(sampleE)):
    sampleE[i] = ((np.random.beta(alphaE, betaE)*scaleE)+locE)

#ANGLE
scaleA = 15

alphaAngle, betaAngle = 1, 7

sampleAngleDeg, sampleAngleRad = [0]*numPoints, [0]*numPoints

for i in range(len(sampleAngleDeg)):
    sampleAngleDeg[i] = (np.random.beta(alphaAngle, betaAngle)*scaleA)
    sampleAngleRad[i] = sampleAngleDeg[i]*np.pi/180

xrangeAngle = np.arange(0, 15, 0.1)
```

```
#SPHERICAL COORDINATE CONVERSION
v0 = [0]*numPoints

c, masse = 1.6e-19, 9.11e-31
for i in range(len(v0)):
    v0[i] = (np.sqrt((2.0*sampleE[i]*c)/masse)*1e-7)        # in cm/ns

#phi = angle from axis (b/w 0,360 deg)
phi = np.random.uniform(low=0, high=360*np.pi/180, size=(numPoints,))

#initilizting vxinit, vyinit, vzinit as size 20
vxinit, vyinit, vzinit = [0]*numPoints, [0]*numPoints, [0]*numPoints

#VX, VY, VZ IN TERMS OF SPHERICAL COORDINATES
for i in range(len(v0)):
    vxinit[i] = v0[i]*np.sin(sampleAngleRad[i])*np.cos(phi[i])
    vyinit[i] = v0[i]*np.sin(sampleAngleRad[i])*np.sin(phi[i])
    vzinit[i] = v0[i]*np.cos(sampleAngleRad[i])
#_____________________________________________________________________________
#                        MAIN SOLVER SETUP
#_____________________________________________________________________________
# time [ns], position [cm], velocity [cm/ns]
def drift3d(t, y):
    #wc = 0.1*(e/m)*B (UNITS: rad/s), e = electric change, m = mass electron, B = Gauss
    wc = 1.75824e-2 # wce  [Grad*s^-1 / Gauss] = [(rad*(1e9 s)^-1)/Gauss] = 1e-9*wc/ B
(rad*s^-1 / Gauss)
    ydot = [0, 0, 0, 0, 0, 0]
    ydot[0] = y[3]
    ydot[1] = y[4]
```

```
    ydot[2] = y[5]
    b0 = Bx(y[2],y[1],y[0])
    b1 = By(y[2],y[1],y[0])
    b2 = Bz(y[2],y[1],y[0])
    ydot[3] = (wc * (b1*y[5] - b2*y[4]))[0]
    ydot[4] = (wc * (b2*y[3] - b0*y[5]))[0]
    ydot[5] = (wc * (b0*y[4] - b1*y[3]))[0]
    return ydot

end=8.25
def electron_detect(t, y): return y[2] - end
electron_detect.terminal = True
electron_detect.direction = 1
#_____
_____
#                                FIXED END NEW SINGLE PORE LOGIC
#_____
_____
#IDEA: HAVE A COLUMN ARRAY MATRIX CALLED ELECTRONDATA, WHERE EACH
ROW IN THE COLUMN MATRIX IS THE SOLUTION TO SOLVE_IVP OF EACH VINIT
electronData = [0]*numPoints

for i in range(len(electronData)):
    electronData[i] = solve_ivp(drift3d, [0, 120], [0, 0, 0, vxinit[i], vyinit[i], vzinit[i]],
t_eval=np.arange(10000)*0.01, events=electron_detect)

#_____
_____
#                                BZ PLOT
#_____
_____
plt.plot(tsz,Bz(tsz,0,0))
```

```
plt.xlabel('z [mm]'), plt.xlim([0,coilLen]), plt.ylim([120, 300]), plt.ylabel('B [Gauss]'), plt.grid()
#_____________________________________________________________________________
#                          XZ and YZ PLOTS
#_____________________________________________________________________________
plt.figure(figsize=(8,14))
plt.subplot(2,1,1)

#XZ PLOT
#plt.plot(electronData[0].y[2],electronData[0].y[0],'b', linewidth=1)
for i in range(len(electronData)):
    plt.plot(electronData[i].y[2], electronData[i].y[0])
plt.xlim([0, coilLen/10]), plt.ylim([-0.05, 0.05]), plt.grid(), plt.xlabel('z [cm]'), plt.ylabel('x [cm]')

plt.subplot(2,1,2)

#YZ PLOT
#plt.plot(electronData[0].y[2],electronData[0].y[0],'b', linewidth=1)
for i in range(len(electronData)):
    plt.plot(electronData[i].y[2], electronData[i].y[1])
plt.xlim([0, coilLen/10]), plt.ylim([-0.05, 0.05]), plt.grid(), plt.xlabel('z [cm]'), plt.ylabel('y [cm]')

#_____________________________________________________________________________
#                          RAW BETA DISTRIBUTION PLOTS
#_____________________________________________________________________________
plt.figure(figsize=(8,14))

#Raw Beta PDF Plots

plt.subplot(1,2,1)
betaEnergy = (beta.pdf(xrangeE, alphaE, betaE, scale=scaleE, loc=locE))
```

```
plt.plot(xrangeE, betaEnergy), plt.xlabel('Electron Energy (eV)'), plt.ylabel('Probability Density Function')

plt.title("Probability Density Function of Initial Electron Energies")


plt.subplot(1,2,2)

betaAngle = (beta.pdf(xrangeAngle, alphaAngle, betaAngle, scale=scaleA))

plt.plot(xrangeAngle, betaAngle), plt.xlabel('Electron Angle (deg)'), plt.ylabel('Probability Density Function')

plt.title("Probability Density Function of Initial Electron Angles")


#_____________________________________________________________________________

#                       ENERGY AND ANGLE DISTRIBUTION PLOTS

#_____________________________________________________________________________


plt.figure(figsize=(8,14))


plt.subplot(2,1,1)

plt.xlim([0, 200]), plt.xlabel('Electron Initial Energy (eV)'), plt.ylabel('Number of Sampled Electrons'), plt.title("Sampled Initial Energy and Angles of Electrons: n=10,000 Electrons")

plt.hist(sampleE, bins=30, color='blue', edgecolor='black')


plt.subplot(2,1,2)

plt.xlim([0, 15]), plt.xlabel('Electron Initial Angle (deg)'), plt.ylabel('Number of Sampled Electrons')

plt.hist(sampleAngleDeg, bins=30, color='blue', edgecolor='black')


#_____________________________________________________________________________

#                       XY Grid Plots @ Z = END

#_____________________________________________________________________________

#plt.ion()

plt.figure(figsize=(8,10))
```

```
rAvgData =  []


count_100, count_200, count_300_plus = 0, 0, 0


#Green, blue, red dot = radius between: [0,100] um, [100,200] um, 200+ um]

for i in range(len(electronData)):

   plt.plot(10000*electronData[i].y_events[0][:,0], 10000*electronData[i].y_events[0][:,1], 'ro'), plt.xlim([-400, 400]), plt.ylim([-400, 400])


rAvgData.append(10000*(np.sqrt((electronData[i].y_events[0][:,0]*electronData[i].y_events[0][:,0])+(electronData[i].y_events[0][:,1]*electronData[i].y_events[0][:,1]))[0]))

   if((rAvgData[i] >= 0) and (rAvgData[i] <= 100)):

      plt.plot(10000*electronData[i].y_events[0][:,0], 10000*electronData[i].y_events[0][:,1], 'go'), plt.xlim([-400, 400]), plt.ylim([-400, 400])

      count_100 += 1

   elif((rAvgData[i] > 100) and (rAvgData[i] <= 200)):

      plt.plot(10000*electronData[i].y_events[0][:,0], 10000*electronData[i].y_events[0][:,1], 'bo'), plt.xlim([-400, 400]), plt.ylim([-400, 400])

      count_200 += 1

   else:

      plt.plot(10000*electronData[i].y_events[0][:,0], 10000*electronData[i].y_events[0][:,1], 'ro'), plt.xlim([-400, 400]), plt.ylim([-400, 400])

      count_300_plus += 1


rAvg = np.average(rAvgData)

rStDev = tstd(rAvgData)

rMin = min(rAvgData)

rMax = max(rAvgData)


print("Average Radius:", rAvg, "um for n = ", len(rAvgData), "data points")
```

```
print("Std Deviation:", rStDev, "(um), Minimum Radius:", rMin, "(um), Maximum Radius:", rMax, "um")

print(count_100, "electrons under 100 um, ", count_200, "Electrons between 100 and 200 um,", count_300_plus, "greater than 300 um")


plt.ylim([-0.05*10000,0.05*10000]), plt.xlim([-0.05*10000,0.05*10000])

plt.grid(), plt.xlabel('X-Position [μm]'), plt.ylabel('Y-Position [μm]'), plt.title("Electron-Hits at Imaging Plane")


#_____________________________________________________________________________

#                    Histogram of Calculated Electron Radii

#_____________________________________________________________________________

plt.figure(figsize=(8,10))

plt.xlim([0, 500]), plt.xlabel('Electron Radius (μm)'), plt.ylabel('Number of Electrons'), plt.title("Simulated Electron Radius Distribution at Imager")

plt.hist(rAvgData, bins=30, color='blue', edgecolor='black')


plt.show()
```

Appendix D

Python Simulation Setup and Parameters

The simulation is first set up by defining a 3-dimensional model space and mesh size. The model space and mesh size used in the model is summarized in Table D.1:

Bounds of X-Dimension	[-10, 10] cm
Bounds of Y-Dimension	[-10, 10] cm
Bounds of Z-Dimension	[0, 100] cm
Number of X-Coordinates	51
Number of Y-Coordinates	51
Number of Z-Coordinates	101

Table D.1: Model space and mesh simulation parameters.

The energy and angle distributions references from literature [2] were traced into Beta statistical distributions. The parameters of the Beta distributions are displayed in Table D.2. In the simulation, the ranges for the initial electron energy and angle are [10 eV, 200 eV] and [0°, 15°]. The x-axes of the Beta distributions are thus scaled by the range of the initial energies and angles. The electron energy probability density function is shifted by +10 eV as low energy electrons do not have sufficient energy to escape the MCP.

	Alpha	Beta
Energy	0.44	1
Angle	1.4	7

Table D.2: Parameters of initial energy and angle beta distributions.

Appendix E

1. PCB Information

The pulsing circuit PCB was designed using Altium PCB software. The Altium circuit schematic and 2D board view are shown in Figures E.1 and E.2. The board was fabricated by JLCPCB with the following options: FR-4 base material, 2 oz. copper weight, 2-layers, and a PCB thickness of 1.6 mm.

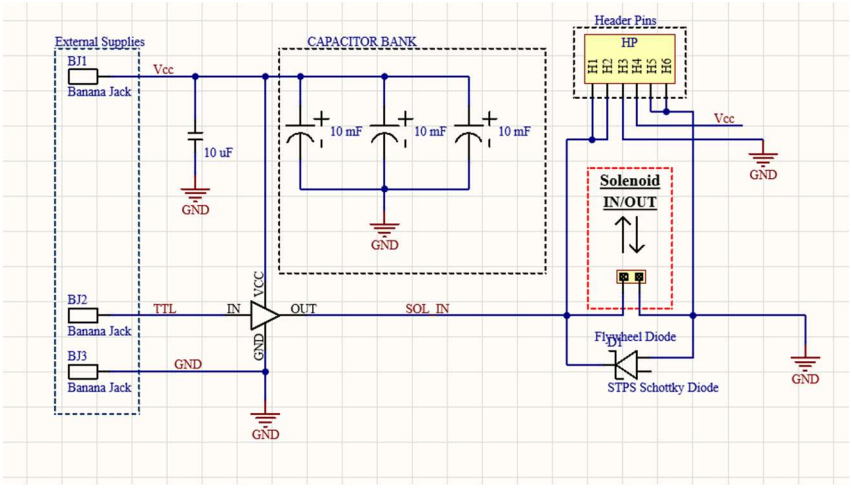

Figure E.1: Altium Board Schematic.

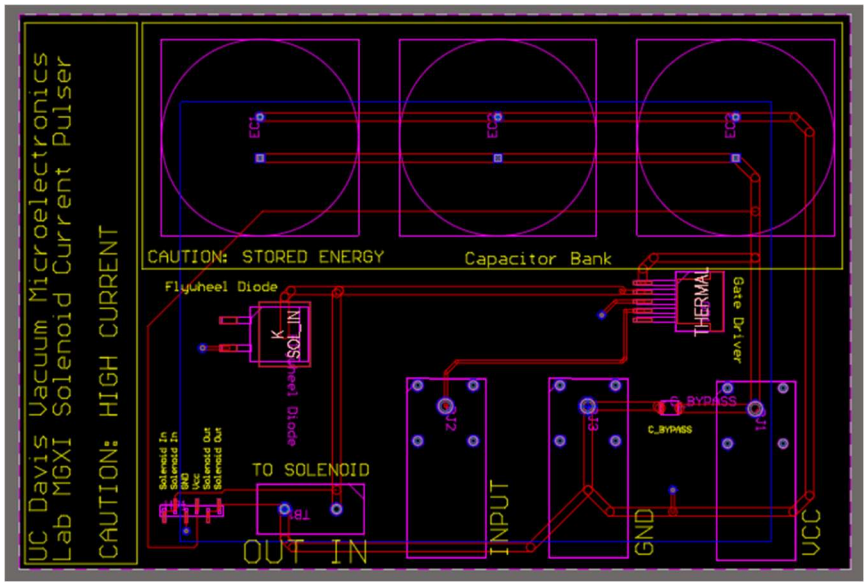

Figure E.2: Final 2D view of Designed Current Pulser PCB.

2. Pulsing Circuit Components

Details of the electrical components used in the PCB can be found in Table E:

Component	Manufacturer	Manufacturer Part #	Description
MOSFET Gate Driver	IXYS Integrated Circuits Division	IXDN630YI	Low-Side Gate Driver IC Non-Inverting TO-263-5
Schottky Diode	STMicroelectronics	STPS41H100C-Y	Automotive low drop power Schottky rectifier
Electrolytic 10 mF Capacitor	Cornell Dubilier / Illinois Capacitor	109LBA050M2EE	10000 µF 50 V Aluminum Electrolytic Capacitors Radial, Can - Snap-In 58.03mOhm @ 120Hz 2000 Hrs @ 85°C
10 µF X7R Capacitor	Murata Electronics	GRJ32ER71H106KE11 X7R	Soft Termination Chip Multilayer Ceramic Capacitors for General Purpose
Terminal Block Connector	On-Shore Technology	OSTT7022150	2 Position Wire to Board Terminal Block Horizontal with Board 0.375" (9.53mm) Through Hole
Banana Jack Connector	Pomona Electronics	73099	Model 73099 Right-Angle Mounting Safety Jack for PCB

Table E: Electrical components used in pulser PCB.

Appendix F

LTSpice Simulation Setup and Parameters

The LTSpice simulation was run under Transient analysis, with a start time of 0ms and stop time of 10ms. The simulation setup was implemented with the following Spice directive:

.tran 0 10m 0s

As mentioned in Section 2.5.2, the MOSFET gate driver was modeled as two voltage-controlled switches. The PMOS is connected to the V(pullup) waveform whereas the NMOS is connected to the V(pulldown) waveform shown in Figure F. The parameters of the input pulses are given in Table F. The two voltage-controlled switches were linked to the input pulses with the following Spice directives:

.model PMOS SW(Ron=0.6 Roff=1Meg Vt=0.9)
.model NMOS SW(Ron=0.45 Roff=1Meg Vt=0.9)

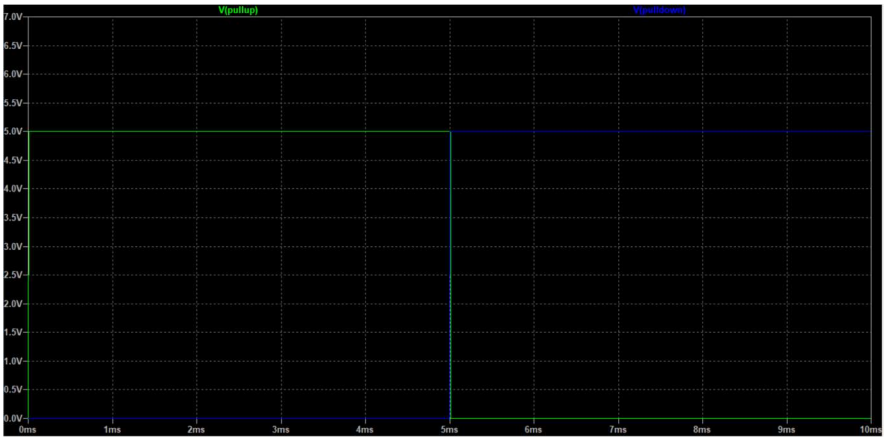

Figure F: Pull-up and pull-down input pulses.

	V_{pullup}	$V_{pulldown}$
Waveform	Pulse	Pulse
Vinitial (V)	0	0
Von (V)	5	5
Tdelay (ms)	.01	5
Trise (ns)	1	1
Tfall (ns)	1	1
Ton (ms)	5	7

Table F: Pull-up and pull-down input voltage source configurations.

Appendix G

Raw Phosphor Plate Beam Images

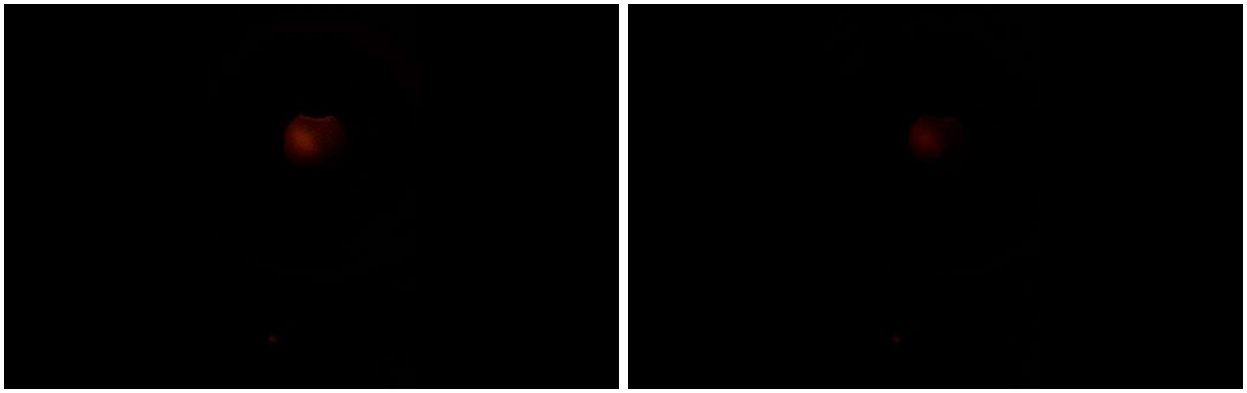

Figure G.1: Raw phosphor plate image under a. test bias 1 (Left) b. test bias 2 (Right).

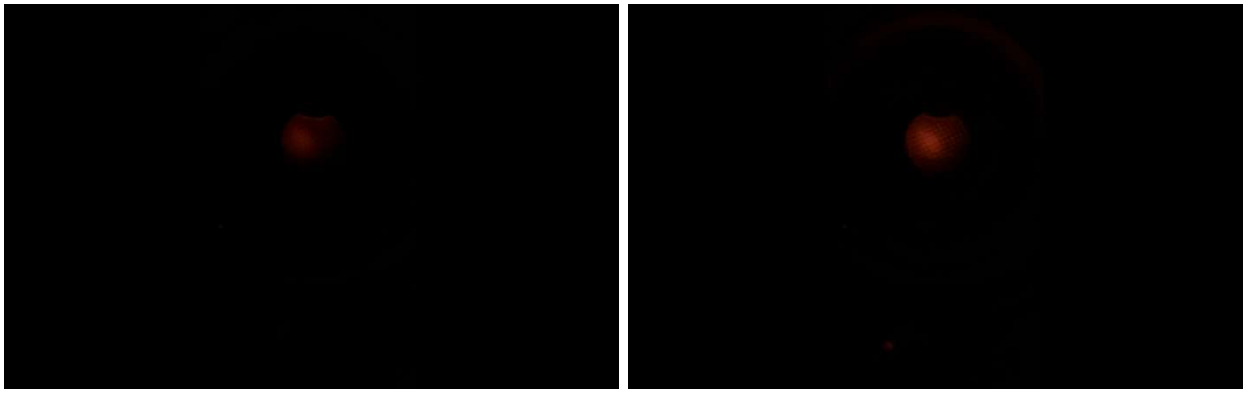

Figure G.2: Raw phosphor plate image under a. test bias 3 (Left) b. test bias 4 (Right).

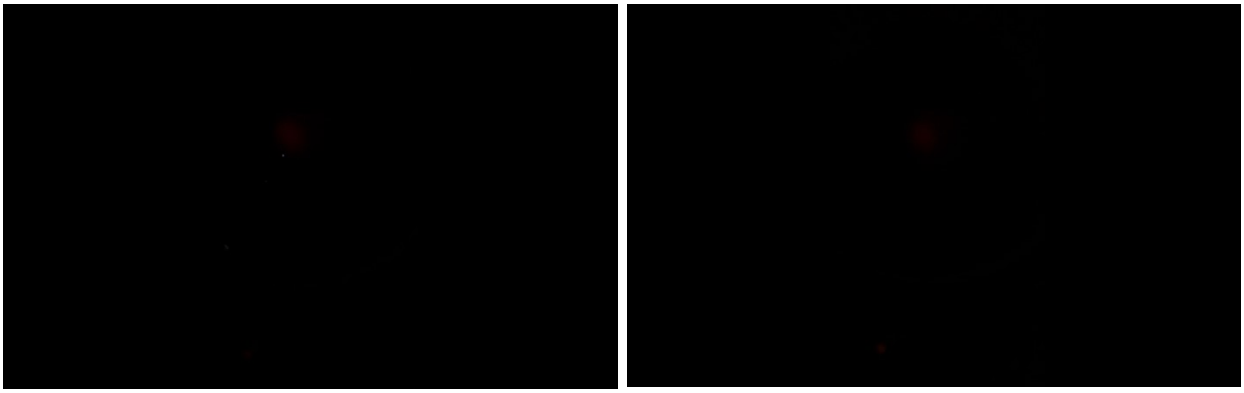

Figure G.3: Raw phosphor plate image under a. test bias 5 (Left) b. test bias 6 (Right).

Figure G.4: Raw phosphor plate image under test bias 7.

Appendix H

Gaussian Fit Parameters

The parameters of the Gaussian intensity fits from Figure 25 are given in Table H:

Test Bias	A	B	C	D
1	1.30	8.48	10.19	2.92
2	0.54	3.81	9.07	3.32
3	0.91	5.40	9.36	2.81
4	1.30	9.71	9.36	3.12
5	0.18	1.34	8.61	3.49
6	0.01	1.17	12.15	3.43
7	2.18	14.90	11.81	3.25

Table H: Electron beam Gaussian intensity fit parameters.

References

[1] J. Ladislas Wiza, “Microchannel plate detectors,” Nuclear Instruments and Methods, vol. 162, no. 1–3, pp. 587–601, Jun. 1979, doi: https://doi.org/10.1016/0029-554x(79)90734-1.

[2] G. J. Price and G. W. Fraser, “Calculation of the output charge cloud from a microchannel plate,” Nuclear Instruments and Methods in Physics Research Section A: Accelerators, Spectrometers, Detectors and Associated Equipment, vol. 474, no. 2, pp. 188–196, Dec. 2001, doi: https://doi.org/10.1016/S0168-9002(01)00880-4.

[3] A. M. Then and C. G. Pantano, “Formation and behavior of surface layers on electron emission glasses,” Journal of Non-Crystalline Solids, vol. 120, no. 1–3, pp. 178–187, Apr. 1990, doi: https://doi.org/10.1016/0022-3093(90)90202-w.

[4] H. E. Meyer, T. Fröhlich, E. Nordhoff, and K. Kuhlmann, “Massenspektrometrie,” Springer eBooks, pp. 359–414, Dec. 2021, doi: https://doi.org/10.1007/978-3-662-61707-6_16.

[5] B. Paszkowski, Electron Optics, 2nd ed. London: Llife, 1968, pp. 5-34.

[6] F. T. Ulaby and Umberto Ravaioli, Fundamentals of Applied Electromagnetics. Pearson, 2015, pp. 237-272.

[7] “HomePage:Finite Element Method Magnetics,” www.femm.info. https://www.femm.info/wiki/HomePage

[8] “The Magpylib Documentation — Magpylib 5.0.0dev documentation,” magpylib.readthedocs.io, Dec. 28, 2023. https://magpylib.readthedocs.io/en/latest/ (accessed Feb. 26, 2024).

[9] “LTspice Information Center | Analog Devices,” Analog.com, 2024. https://www.analog.com/en/resources/design-tools-and-calculators/ltspice-simulator.html